ARTICLE

Minibrain kinase and calcineurin coordinate activity-dependent bulk endocytosis through synaptojanin

Yi-Jheng Peng[1,2]*, Junhua Geng[1]*, Ying Wu[1], Cristian Pinales[3], Jennifer Langen[1], Yen-Ching Chang[1], Christopher Buser[3], and Karen T. Chang[1,2,4]

Neurons use multiple modes of endocytosis, including clathrin-mediated endocytosis (CME) and activity-dependent bulk endocytosis (ADBE), during mild and intense neuronal activity, respectively, to maintain stable neurotransmission. While molecular players modulating CME are well characterized, factors regulating ADBE and mechanisms coordinating CME and ADBE activations remain poorly understood. Here we report that Minibrain/DYRK1A (Mnb), a kinase mutated in autism and up-regulated in Down's syndrome, plays a novel role in suppressing ADBE. We demonstrate that Mnb, together with calcineurin, delicately coordinates CME and ADBE by controlling the phosphoinositol phosphatase activity of synaptojanin (Synj) during varying synaptic demands. Functional domain analyses reveal that Synj's 5′-phosphoinositol phosphatase activity suppresses ADBE, while SAC1 activity is required for efficient ADBE. Consequently, Parkinson's disease mutation in Synj's SAC1 domain impairs ADBE. These data identify Mnb and Synj as novel regulators of ADBE and further indicate that CME and ADBE are differentially governed by Synj's dual phosphatase domains.

Introduction

The rapid uptake and recycling of synaptic vesicle (SV) membrane and protein components are essential for reliable synaptic transmission across a wide range of neuronal activities (Saheki and De Camilli, 2012; Soykan et al., 2016; Chanaday et al., 2019). Defects in SV retrieval can thus have deleterious consequences on neuronal survival and function, and are associated with numerous neurological disorders (Abeliovich and Gitler, 2016; Li and Kavalali, 2017; Bonnycastle et al., 2021). There are multiple proposed modes of SV retrieval from the plasma membrane that replenish distinct functional SV pools (Saheki and De Camilli, 2012; Soykan et al., 2016; Chanaday et al., 2019). The best understood SV retrieval mode is clathrin-mediated endocytosis (CME), in which clathrin assembly at the plasma membrane is essential (Takei et al., 1996; Gad et al., 1998; Granseth et al., 2006). CME mainly operates during mild or moderate neuronal activity to retrieve the active cycling vesicle pool, also known as the exo/endo cycling pool (ECP; Kuromi and Kidokoro, 1998; Delgado et al., 2000; Kuromi and Kidokoro, 2000; Rizzoli and Betz, 2005; Granseth et al., 2006; Zhu et al., 2009; Cheung et al., 2010). During intense neuronal activity, a clathrin-independent

endocytosis (CIE) mode, also known as activity-dependent bulk endocytosis (ADBE), is the predominant mode that rapidly retrieves large areas of the synaptic membrane (Clayton et al., 2008; Clayton and Cousin, 2009b; Soykan et al., 2016). Functional SVs are then regenerated from endosomes to replenish the reserve pool vesicles (RPs), which are mobilized during high-frequency stimulation (Richards et al., 2000; Rizzoli and Betz, 2005; Clayton and Cousin, 2009b; Clayton et al., 2010; Soykan et al., 2016). While elegant studies have shed light on mechanisms regulating CME, molecular players modulating ADBE, especially those coordinating the relative activations of CME and ADBE during different stimulation conditions, remain poorly understood.

One key mechanism that tightly regulates and fine-tunes CME is the phosphorylation of multiple endocytic proteins by kinases (Slepnev et al., 1998; Rizzoli, 2014). For example, the Minibrain (Mnb) kinase (also known as DYRK1A kinase) has been shown to phosphorylate synaptojanin (Synj; Chen et al., 2014; Geng et al., 2016), a phosphoinositol phosphatase (PPase) important for CME (McPherson et al., 1996; Cremona et al., 1999;

[1]Zilkha Neurogenetic Institute, Keck School of Medicine, University of Southern California, Los Angeles, CA; [2]Neuroscience Graduate Program, University of Southern California, Los Angeles, CA; [3]Oak Crest Institute of Science, Monrovia, CA; [4]Department of Physiology & Neuroscience, Keck School of Medicine, University of Southern California, Los Angeles, CA.

*Y-J. Peng and J. Geng contributed equally to this paper; Correspondence to K.T. Chang: changkt@usc.edu; J. Geng's present address is School of Life Science and Technology, Southeast University, Nanjing, Jiangsu, China;

Harris et al., 2000; Verstreken et al., 2003; Mani et al., 2007). Synj contains a 5′-PPase domain that converts phosphatidylinositol 4,5-bisphosphate [PI(4,5)P2] to phosphatidylinositol 4-phosphate [PI(4)P], and a SAC1 domain that converts PI(4)P to phosphatidylinositol (PI; McPherson et al., 1996). Phosphorylation of Synj by Mnb enhances Synj's 5′-PPase activity and alters Synj's interaction with endophilin A, thereby promoting recycling of ECP through CME, presumably by enhancing the rate of clathrin uncoating (Chen et al., 2014; Geng et al., 2016). Although not well understood, kinase and phosphatase functions have also been implicated in the regulation of ADBE. Phosphorylation of dynamin by GSK-3 has been shown to activate ADBE (Clayton et al., 2010). The calcium/calmodulin-dependent phosphatase calcineurin (CaN) has also been reported to be a key protein activating ADBE (Clayton et al., 2009; Cheung and Cousin, 2013), likely through dephosphorylation of dynamin. However, recent studies show that dynamin knockouts can undergo ADBE in both flies and mice (Kasprowicz et al., 2008; Wu et al., 2014b), suggesting that dynamin may be dispensable for ADBE. There is thus a significant gap in our understanding of the protein networks in ADBE and the molecular targets downstream of kinases and phosphatases essential for ADBE activation.

In this study, we present evidence that Mnb/DYRK1A and Synj are novel regulators of ADBE. We show that Mnb, together with CaN, regulates the phosphorylation status of Synj to coordinate CME and ADBE activations during different stimuli. Specifically, Mnb suppresses ADBE but promotes CME during moderate neuronal activity through phosphorylation of Synj; dephosphorylation of Synj by CaN during intense stimulation then activates ADBE. Examination of Synj functional domains revealed that Synj's 5′-PPase domain suppresses ADBE, while Synj's SAC1 activity is required for efficient ADBE. These results further imply that differential regulation of phosphoinositides by Synj's dual phosphatase domains is a key mechanism controlling ADBE activation.

Results

Mnb kinase suppresses clathrin-independent ADBE
Mnb was previously shown to be required for efficient CME (Geng et al., 2016), but its role in CIE is not known. To separately examine CME and CIE endocytosis, we performed FM1-43 dye uptake assays in the presence or absence of a clathrin inhibitor called chlorpromazine (CPZ) using different stimulation conditions. Published reports indicate that high KCl stimulation in the presence of low Ca^{2+} (hereafter called CME protocol) activates CME but not CIE at the fly neuromuscular junction (NMJ; Kuromi and Kidokoro, 2005; Verstreken et al., 2005; Verstreken et al., 2008; Yao et al., 2017), whereas high KCl in the presence of CPZ activates CIE (hereafter referred to as CIE protocol; Kasprowicz et al., 2008; Fig. 1 A). When using the CME protocol, FM1-43 staining showed a doughnut-shaped pattern with the dye located at the periphery of the bouton (Fig. 1 B), consistent with ECP vesicle distribution (Kuromi and Kidokoro, 1998; Verstreken et al., 2005). When stimulated with the CIE protocol, FM1-43 staining instead appeared punctate and located

in subbutonic regions previously shown to correspond to bulk membrane uptake (Kasprowicz et al., 2008; Fig. 1 B, arrowheads). We also validated the efficacy of the CME and CIE protocols by examining synaptic boutons using transmission EM (TEM). Stimulation of the NMJ using the CME protocol failed to elicit a significant increase in the number of bulk endosomes >80 nm (Fig. S1, A and B), consistent with a previous report that this protocol does not trigger bulk endocytosis (Yao et al., 2017). On the other hand, the CIE protocol caused an accumulation of membrane cisternae >80 nm (size of the observed endosomes ranged from 81 to 250 nm), suggesting that our CIE induction protocol effectively triggered clathrin-independent bulk endocytosis (Fig. S1, A and B). Together, these results confirm that the CME and CIE stimulation protocols reliably promote CME and CIE, respectively.

Next, we monitored CME and CIE activations in mnb^1, a mutant with a point mutation in the kinase domain that severely diminishes Mnb kinase activity and renders the protein unstable (Tejedor et al., 1995; Ori-McKenney et al., 2016). mnb^1 displayed reduced FM1-43 uptake when stimulated using the CME protocol, consistent with a previous report that Mnb promotes CME (Chen et al., 2014). Surprisingly, when stimulated using the CIE protocol, mnb^1 showed higher FM1-43 loading intensity and larger internalized membrane area (normalized to bouton area) when clathrin was blocked (Fig. 1, B–D). Overexpression of Mnb (mnb OE) in neurons alone led to opposite results (Fig. 1, B–D). Up-regulation of Mnb in mnb^1 rescued the phenotypes, confirming that Mnb is responsible for the observed changes. Together, these results imply that Mnb normally functions to promote efficient CME but suppresses CIE. Interestingly, because clathrin was blocked in all genotypes when monitoring CIE, the increase in FM1-43 uptake seen in mnb^1 cannot be due simply to a default activation of CIE when CME is inactivated, but rather suggests that loss of Mnb actively enhances CIE.

To avoid the potential nonspecific effects of clathrin inhibitors (Dutta et al., 2012; Guo et al., 2015), we genetically blocked clathrin function by (1) expressing a dominant-negative construct of clathrin-heavy chain (chc^{DN}) previously shown to inhibit clathrin triskeleton assembly and clathrin function (Liu et al., 1998), and (2) knocking down a clathrin adaptor protein, like AP-180 (Lap), important for clathrin localization to the synaptic terminals of fly NMJ (Zhang et al., 1998). Stimulation of either chc^{DN} or lap-RNAi NMJs using high KCl (without CPZ) caused an increase in boutons with distinct punctate FM1-43–positive inclusions (Fig. S1, C and E), similar to that observed when clathrin was blocked using CPZ. When chc^{DN} or lap-RNAi was expressed in mnb^1 background, KCl stimulation further increased the number of boutons with punctate membrane inclusions (Fig. S1, D and F), suggesting that Mnb normally suppresses CIE.

The punctate spots labeled by FM1-43 using the CIE protocol correlated with bulk membrane uptake (Kasprowicz et al., 2008), implying that Mnb may modulate bulk endocytosis in an activity-dependent manner. To assay the role of Mnb in ADBE under a more physiological condition (without clathrin inhibition), we monitored the ability of synapses to take up a nonlipophilic, fluorescently tagged dextran (10-kD tetramethylrhodamine-dextran) during electrical stimulation. 10-kD dextran is a fluid phase
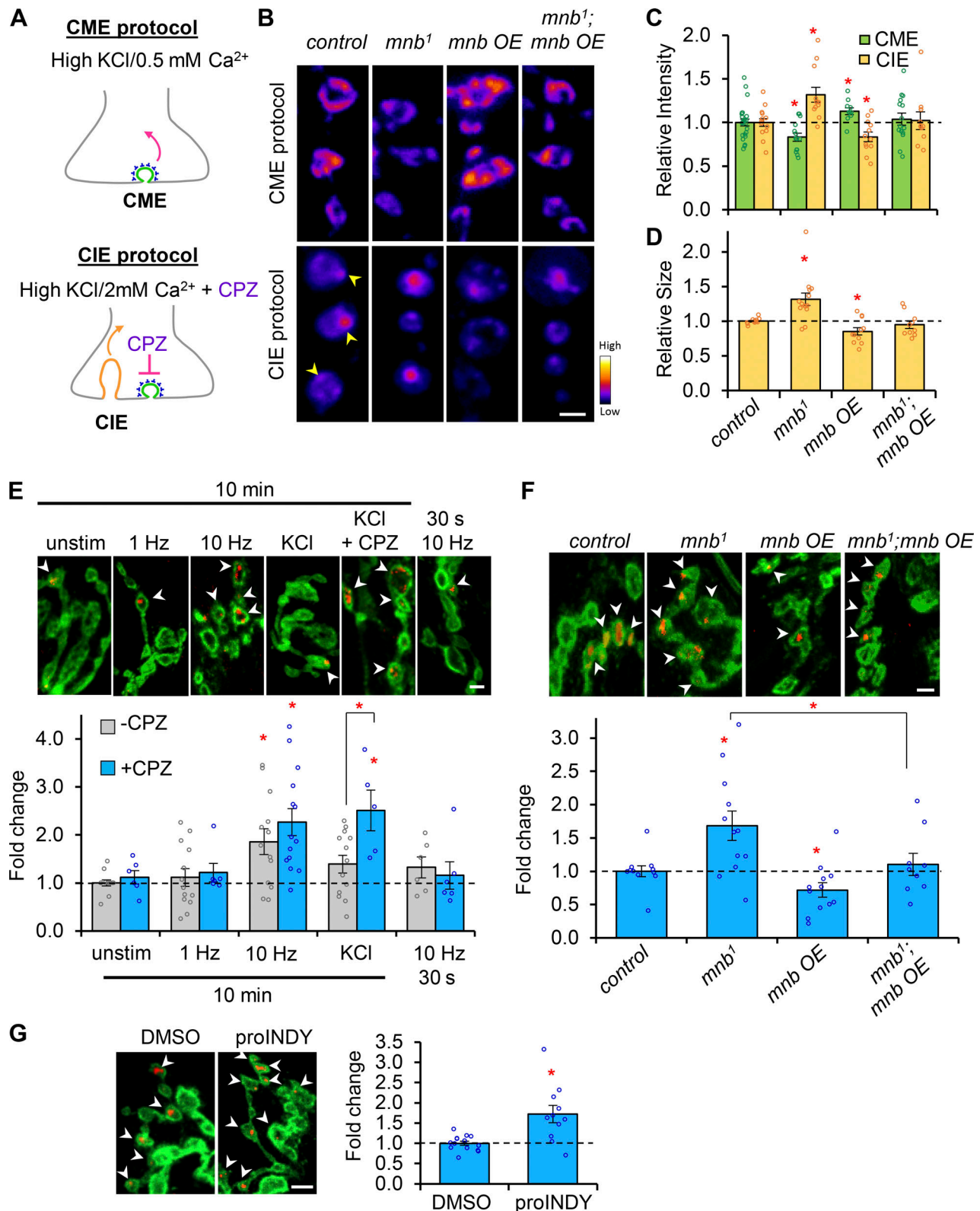
Peng et al.
Molecular mechanism coordinating endocytosis modes

Journal of Cell Biology   2 of 18
https://doi.org/10.1083/jcb.202011028

Figure 1. **Mnb suppresses ADBE but promotes CME. (A)** Schematic of stimulation protocols activating CME (top) and CIE (bottom). **(B)** Representative images of NMJ loaded with FM1-43 using the CME or CIE protocol as indicated (pseudo-colored). Arrowheads highlight the punctate membrane labeling indicative of bulk endocytosis. **(C)** Relative FM1-43 loading intensity normalized to control NMJ (CME: control, $n = 26$; mnb^1, $n = 14$; mnb OE, $n = 10$; mnb^1; mnb OE, $n = 15$; CIE: control, $n = 12$; mnb^1, $n = 14$; mnb OE, $n = 11$; mnb^1; mnb OE, $n = 10$). **(D)** Normalized internalized membrane area seen following FM1-43 loading using the CIE protocol (control, $n = 12$; mnb^1, $n = 14$; mnb OE, $n = 11$; mnb^1; mnb OE, $n = 10$). **(E)** Representative images of control NMJ loaded with fluorescent dextran during different stimulation conditions. Quantification of dextran index was determined by counting the number of boutons with dextran uptake (red) and normalizing to the total bouton number (highlighted by HRP, green). Fold change was normalized to unstimulated (unstim) control (–CPZ: unstimulated:

n = 12; 1 Hz, n = 13; 10 Hz, n = 13; KCl, n = 13; 10 Hz 30 s, n = 6. +CPZ: unstimulated: n = 6; 1 Hz, n = 6; 10 Hz, n = 14; KCl, n = 5; 10 Hz 30 s, n = 6. **(F)** Mnb suppresses ADBE assayed by dextran uptake following 10 Hz stimulation for 10 min (control, n = 11; mnb[1], n = 12; mnb OE, n = 12; mnb[1]; mnb OE, n = 9). **(G)** Acute inhibition of Mnb by proINDY enhances dextran uptake. NMJs were preincubated with DMSO (n = 14) or proINDY (n = 11) and stimulated at 10 Hz for 10 min. Scale bar = 2 µm in B and E–G. *, P < 0.05 compared with control or as indicated. n values indicate the number of NMJs assayed. All values represent mean ± SEM.

marker that does not bind to the plasma membrane and has been shown to selectively label bulk uptake, as this mode retrieves a larger volume of extracellular fluid to allow visualization of the dye (Clayton and Cousin, 2009a; Uytterhoeven et al., 2011). We monitored dextran uptake using various stimulation conditions and determined the dextran uptake index by counting boutons with fluorescent-dextran uptake and normalizing it to the total bouton number. This parameter, rather than the average dextran intensity, has been shown to more accurately report the extent of bulk uptake in hippocampal neurons (Clayton and Cousin, 2009a). We found that only intense stimulation (10 Hz for 10 min) and high KCl stimulation in the presence of CPZ could increase dextran uptake above unstimulated control (Fig. 1 E). In contrast, mild stimulation (1 Hz for 10 min), high KCl stimulation without CPZ, or moderate stimulation (10 Hz for 30 s) all failed to elevate dextran uptake (Fig. 1 E). These data are consistent with selective labeling of ADBE by dextran.

Having established that intense stimulation (10 Hz for 10 min) triggers ADBE in wild-type NMJ, we next monitored ADBE in mnb[1]. We found that mnb[1] displayed significantly higher dextran uptake; mnb OE showed reduced dextran uptake; and expression of Mnb in mnb[1] restored dextran uptake to control level (Fig. 1 F). Consistent with the FM1-43 loading experiments, these data reveal that Mnb normally suppresses ADBE. Since Mnb is a kinase that also affects synaptic growth (Chen et al., 2014), we evaluated whether Mnb is acutely required during neuronal activity, or rather developmental defects contribute to altered endocytosis. We transiently blocked Mnb kinase activity using proINDY, a selective and cell-permeable inhibitor of DYRK1A (Ogawa et al., 2010; Chen et al., 2014). Fig. 1 G shows that acute inhibition of Mnb by proINDY was sufficient to significantly elevate dextran uptake following 10-Hz, 10-min stimulation, suggesting that Mnb kinase acts during neuronal activity to inhibit ADBE.

To further verify that Mnb modulates ADBE, we used TEM to monitor bulk uptake following stimulation of individual synapses at 10 Hz for 10 min (Fig. 2 A). Consistent with dextran labeling experiments, mnb[1] synapses displayed an increase in the number of cisternae >80 nm in diameter (Fig. 2 B), suggesting enhanced bulk membrane endocytosis (Yao et al., 2017). Interestingly, 10-Hz stimulation increased SV density in control but not in mnb[1] synapses (Fig. 2 C). This increase in SV density immediately following prolonged high-frequency stimulation had been reported previously and was shown to be due to enhanced endocytosis coupled with SV regeneration (Akbergenova and Bykhovskaia, 2009b). The observation that mnb[1] did not show an increase in SV density following stimulation is consistent with the essential role of Mnb in maintaining SV endocytosis (Chen et al., 2014), and further implies that despite increased bulk uptake, Mnb may also affect the regeneration of

SVs. We found that the average size of SVs in mnb[1] is larger and more variable than control in unstimulated synapses, consistent with increased mEPSP amplitude reported earlier (Chen et al., 2014; Fig. S2, A–C). The size of SV immediately following stimulation (aside from the large cisternae) was the same between control and mnb[1], suggesting that Mnb may alter the size of SV during biogenesis but not during SV endocytosis. Note that in addition to electrical stimulation, we also monitored ADBE following high KCl depolarization (90 mM KCl/2 mM Ca^{2+}, 10 min), an established condition known to activate ADBE at the Drosophila NMJ (Yao et al., 2017; Li et al., 2020). Substantially more bulk endosomes >80 nm were observed compared with electrical stimulation (Fig. S2, D and E), consistent with high potassium depolarization being stronger than electrical stimulation (Akbergenova and Bykhovskaia, 2009a). Regardless, mnb[1] still displayed a significant increase in the number of bulk endosomes compared with stimulated control (Fig. S2, D and E), confirming that loss of Mnb enhances ADBE.

Mnb suppresses ADBE through phosphorylation of Synj at S1029

How does Mnb suppress ADBE? We postulated that Mnb inhibits ADBE through phosphorylation of Synj. This is based on reports that (1) Synj is a substrate of Mnb in vitro and in vivo (Chen et al., 2014; Geng et al., 2016); and (2) Mnb-dependent phosphorylation of Synj at the S1029 site enhances ECP vesicle uptake, but dephosphorylated Synj promotes the recycling of the RP vesicles (Geng et al., 2016). As ECP and RP are recycled through CME and ADBE pathways, respectively (Richards et al., 2000; Rizzoli and Betz, 2005; Clayton and Cousin, 2009b; Cheung et al., 2010), this raises the possibility that phosphorylation of Synj at S1029 can differentially regulate ADBE. The role of Synj in CME has been established by numerous elegant studies (Cremona et al., 1999; Harris et al., 2000; Verstreken et al., 2003; Mani et al., 2007), but how phosphorylation of Synj at S1029 modulates CME and CIE remains unclear. We monitored FM1-43 uptake using the CME and CIE protocols. Fig. 3 A shows that synj[1]/synj[2], a functional null mutant (Verstreken et al., 2003; Vanhauwaert et al., 2017), displayed reduced FM1-43 dye uptake following stimulation using either the CME or CIE protocol, whereas expression of synj[wt] in synj mutant restored FM1-43 load to normal. These results confirm that Synj is necessary for efficient CME and CIE, and are consistent with a requirement for Synj in all modes of endocytosis (Mani et al., 2007). We next determined how the phosphorylation status of Synj regulates CME and CIE. Expression of the phospho-null Synj (synj[S1029A]) in synj mutant did not rescue FM1-43 load stimulated using the CME protocol, but significantly enhanced FM1-43 uptake using the CIE protocol. Expression of phosphomimetic Synj (synj[S1029E]) rescued FM1-43 load stimulated
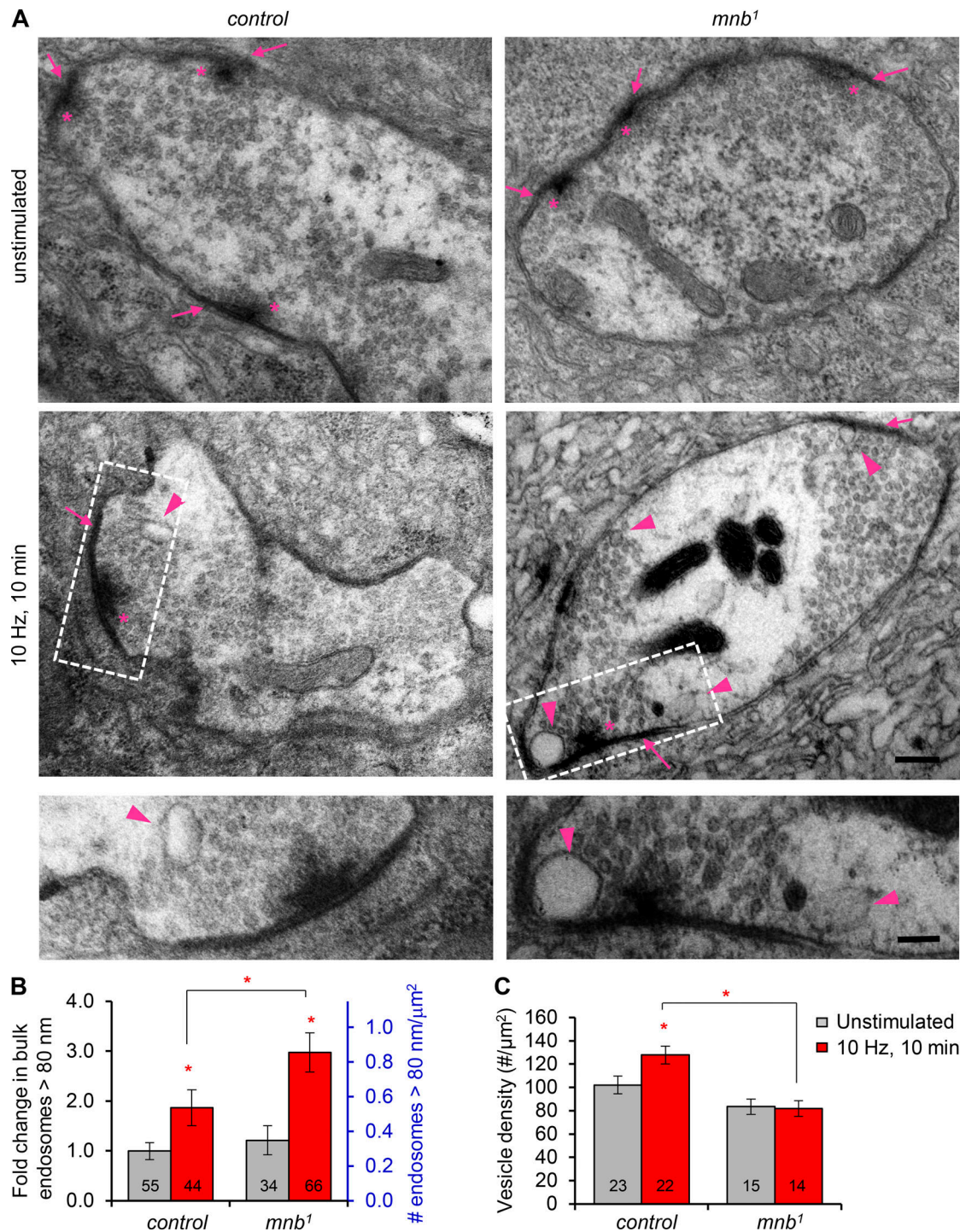
Figure 2. **TEM analyses of *control* and *mnb¹* following electrical stimulation demonstrate that Mnb suppresses ADBE. (A)** Representative TEM images of NMJ boutons. 10-Hz stimulation for 10 min was used to trigger ADBE. Arrowheads indicate bulk-like cisternae >80 nm in diameter. * highlights the T-bar, and arrows point to synaptic thickenings in the active zone area. Scale bar = 200 nm. White boxed area is magnified in the lower panel with scale bar = 100 nm. **(B)** Quantification of the number of bulk cisternae >80 nm in diameter normalized to bouton area (right y axis). Fold-change is calculated by comparing to unstimulated control (left y axis). Number of boutons analyzed per genotype is indicated in the graph. **(C)** Quantification of average SV density normalized to bouton area. Number of boutons analyzed per genotype is indicated in the graph. To obtain accurate numbers of SV, only images with clearly countable SVs are analyzed. *, $P < 0.05$ compared with unstimulated control or as indicated.
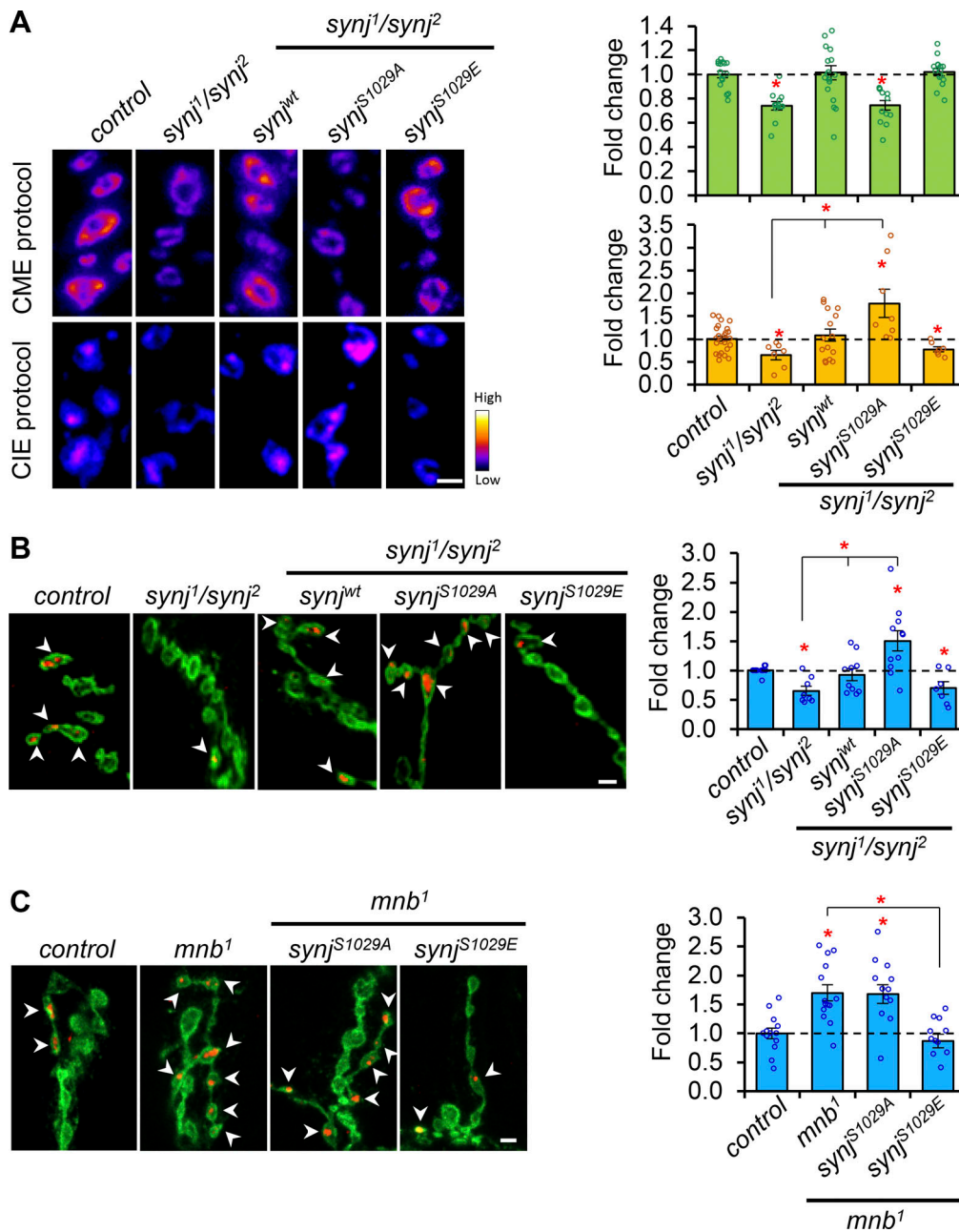
Figure 3. **Phosphorylation status of Synj at S1029 regulates ADBE. (A)** Representative images of NMJ loaded with FM1-43 using the CME or CIE protocol as indicated (pseudo-colored). Phosphorylated Synj promotes CME whereas dephosphorylated Synj promotes CIE. Graph shows fold-change in FM1-43 uptake intensity normalized to control. For CME (upper graph): control, $n = 17$; synj mutant, $n = 12$. In synj mutant background: synj^WT, $n = 18$; synj^S1029A, $n = 13$; synj^S1029E, $n = 15$. For CIE (lower graph): control, $n = 24$; synj mutant, $n = 7$. In synj mutant background: synj^WT, $n = 15$; synj^S1029A, $n = 8$; synj^S1029E, $n = 7$. **(B)** Synj is required for efficient ADBE. Dextran uptake (red) was normalized to the total number of boutons outlined by HRP staining (green) following 10-Hz stimulation for 10 min (control, $n = 16$; synj mutant, $n = 8$; synj mutant background: synj^WT, $n = 10$; synj^S1029A, $n = 11$; synj^S1029E, $n = 7$). **(C)** Phosphomimetic Synj suppresses enhanced dextran uptake in mnb^1 (control, $n = 13$; mnb^1, $n = 14$; mnb^1 background: synj^S1029A, $n = 12$; synj^S1029E, $n = 11$). Scale bar = 2 µm for all figure panels. n values indicate the number of NMJ assayed. All values represent mean ± SEM *, $P < 0.05$ compared with control or as indicated.

by CME protocol but not if stimulated by CIE protocol (Fig. 3 A). Together, these results suggest that phosphorylated Synj predominantly participates in CME, while the dephosphorylated form of Synj promotes CIE.

Next, we monitored ADBE using dextran dye and 10-Hz stimulation. Synj mutant showed diminished dextran dye uptake, while expression of synj^wt in synj mutant restored dextran

loading to normal, indicating that Synj is required for efficient ADBE. Expression of synj^S1029A significantly elevated dextran uptake, but synj^S1029E failed to rescue synj mutant (Fig. 3 B). Collectively, our data suggest that (1) Synj is important for clathrin-independent ADBE; (2) the phosphorylation status of Synj at S1029, a site phosphorylated by Mnb, differentially directs endocytosis pathways; and (3) dephosphorylated form of

Synj promotes ADBE, while phosphorylated Synj either cannot activate ADBE or may act to suppress ADBE.

We hypothesized that if phosphorylated Synj suppresses ADBE, replenishing the level of phosphorylated Synj in mnb^1 should restore ADBE to normal. Indeed, expression of the phosphomimetic $synj^{S1029E}$ in mnb^1 reduced dextran uptake index to control levels, whereas expression of the phospho-null $synj^{S1029A}$ displayed the same elevated dextran uptake as mnb^1 (Fig. 3 C). These results reveal that phosphorylation of Synj at S1029 by Mnb actively suppresses ADBE.

Prolonged intense stimulation abolishes activity-dependent phosphorylation of Synj by Mnb

The findings that Mnb phosphorylates Synj to promote CME but dephosphorylation of Synj is required to activate ADBE raised the following questions: (1) Is Synj dephosphorylated during conditions that trigger ADBE? (2) What is the phosphatase responsible for Synj dephosphorylation? To determine Synj phosphorylation status during conditions that trigger ADBE, we monitored phospho-Synj levels using an antibody sensitive to phosphorylation at S1029 (Geng et al., 2016). Stimulation at 1 Hz for 30 s or 10 min did not alter the level of pSynj (Fig. S3 A); high-frequency stimulation at 10 Hz for 30 s instead resulted in a moderate but statistically significant increase in phospho-Synj level in control but not in mnb^1, indicating that the increase in phospho-Synj is dependent on Mnb. However, prolonged stimulation at 10 Hz (10 min) abolished this increase in phospho-Synj level, suggesting that a phosphatase had been activated (Fig. 4 A). Notably, the condition that triggers Synj dephosphorylation is also one that activates ADBE, further supporting the notion that acute dephosphorylation of Synj during intense activity promotes ADBE.

Synj is dephosphorylated by CaN at S1029 during intense neuronal activity

Intense neuronal activity has been shown to increase intracellular calcium level and activate CaN (Marks and McMahon, 1998; Wu et al., 2009). CaN is important for all modes of endocytosis including ADBE, but whether it is activated in response to different stimuli in vivo at the *Drosophila* NMJ has not been examined. To this end, we generated transgenic flies expressing a fluorescence resonance energy transfer (FRET)–based CaN activity reporter (Mehta et al., 2014), cyto-CaNAR2, along with the Ca^{2+} indicator RCaMP in neurons (Fig. 4 B). We found that 10-Hz stimulation increased presynaptic FRET signal (YFP/CFP) that reached significance by 2 min as compared with unstimulated control, indicating increased CaN activity. This increase is also accompanied by higher Ca^{2+} level as monitored by RCaMP Ca^{2+} indicator. On the other hand, 1-Hz stimulation triggered only a moderate increase in Ca^{2+} level and did not elicit detectable change in CaN activity (Fig. 4 B). To ensure that cyto-CaNAR2 is a reliable reporter for CaN activity, we also stimulated the NMJ at 10 Hz in the presence of FK506, a selective CaN inhibitor. FK506 effectively blocked the increase in FRET signal without affecting Ca^{2+} influx (Fig. S3 B). Together, our data demonstrate that stronger stimulation efficiently activates CaN at the *Drosophila* NMJ.

We next addressed whether CaN dephosphorylates Synj during condition that activates ADBE. First, we confirmed that CaN directly dephosphorylated Synj at S1029 in vitro (Fig. 5 A), and dephosphorylation of Synj by CaN diminished Synj's 5′-PPase activity (Fig. 5 B). Next, we took a genetic approach to regulate CaN activity in neurons by using RNAi against the calcineurin B gene, an obligatory subunit necessary for CaN activity (CaN-RNAi; Klee et al., 1998), or by expressing a constitutively active CaN with its autoinhibitory domain deleted (CaN^{Act}; Shaw and Chang, 2013). Manipulating CaN levels in neurons altered the basal levels of phospho-Synj at the synapse in a pattern consistent with CaN as an in vivo phosphatase of Synj (Fig. 5 C). We also monitored the levels of phospho-Synj in synapses following 10-Hz stimulation. Expression of CaN-RNAi did not affect acute increase in pSynj during moderate activity (30 s) but blocked dephosphorylation of Synj during long-term stimulation (10 min), normally seen in control NMJs (Fig. 5 D), suggesting that CaN is responsible for Synj dephosphorylation during prolonged intense neuronal activity. Expression of a constitutively active CaN showed reduced phospho-Synj level but was no longer sensitive to stimulation conditions (Fig. 5 D). Together, these data reveal that CaN and Mnb coordinate the phosphorylation status of Synj during different neuronal activity.

CaN dephosphorylation of Synj at S1029 is required for efficient ADBE

To understand the role of CaN in regulating ADBE at the fly NMJ, we monitored bulk endocytosis using the dextran uptake assay. Expression of CaN-RNAi significantly reduced dextran uptake, while expression of CaN^{Act} enhanced it, indicating that CaN is required for efficient ADBE (Fig. 5 E). As CaN likely has multiple synaptic targets in addition to Synj, we next tested whether altering Synj phosphorylation status downstream of CaN is sufficient to affect ADBE. Expression of phospho-defective $Synj^{S1029A}$ construct in CaN-RNAi flies significantly elevated ADBE, whereas expression of phosphomimetic $Synj^{S1029E}$ did not rescue (Fig. 5 F). Together, these results imply that the presence of dephosphorylated form of Synj is sufficient to bypass the requirement for CaN for efficient ADBE.

Synj's dual phosphatase domains differentially regulate endocytosis

How does Synj regulate ADBE? Several studies suggest that the phosphoinositide metabolism is important for regulating endocytic events (Cremona et al., 1999; He et al., 2017), and that $PI(4,5)P_2$ microdomain forms at the periactive zone in response to strong stimuli (Li et al., 2020). Synj is a key regulator of $PI(4,5)P_2$ content at the synapse through its 5′-PPase domain (Cremona et al., 1999; Di Paolo and De Camilli, 2006). Dephosphorylation of Synj at S1029 reduces Synj's 5′-PPase activity, leading to elevated $PI(4,5)P_2$ content at the synapse (Geng et al., 2016). On the other hand, phosphorylation status at S1029 does not affect Synj's SAC1 activity (Fig. S4 A). Since mnb^1 and $Synj^{S1029A}$ NMJs both have enhanced ADBE and elevated levels of $PI(4,5)P_2$ (Chen et al., 2014; Geng et al., 2016), we postulated that $PI(4,5)P_2$ elevation underlies the observed increase in ADBE.
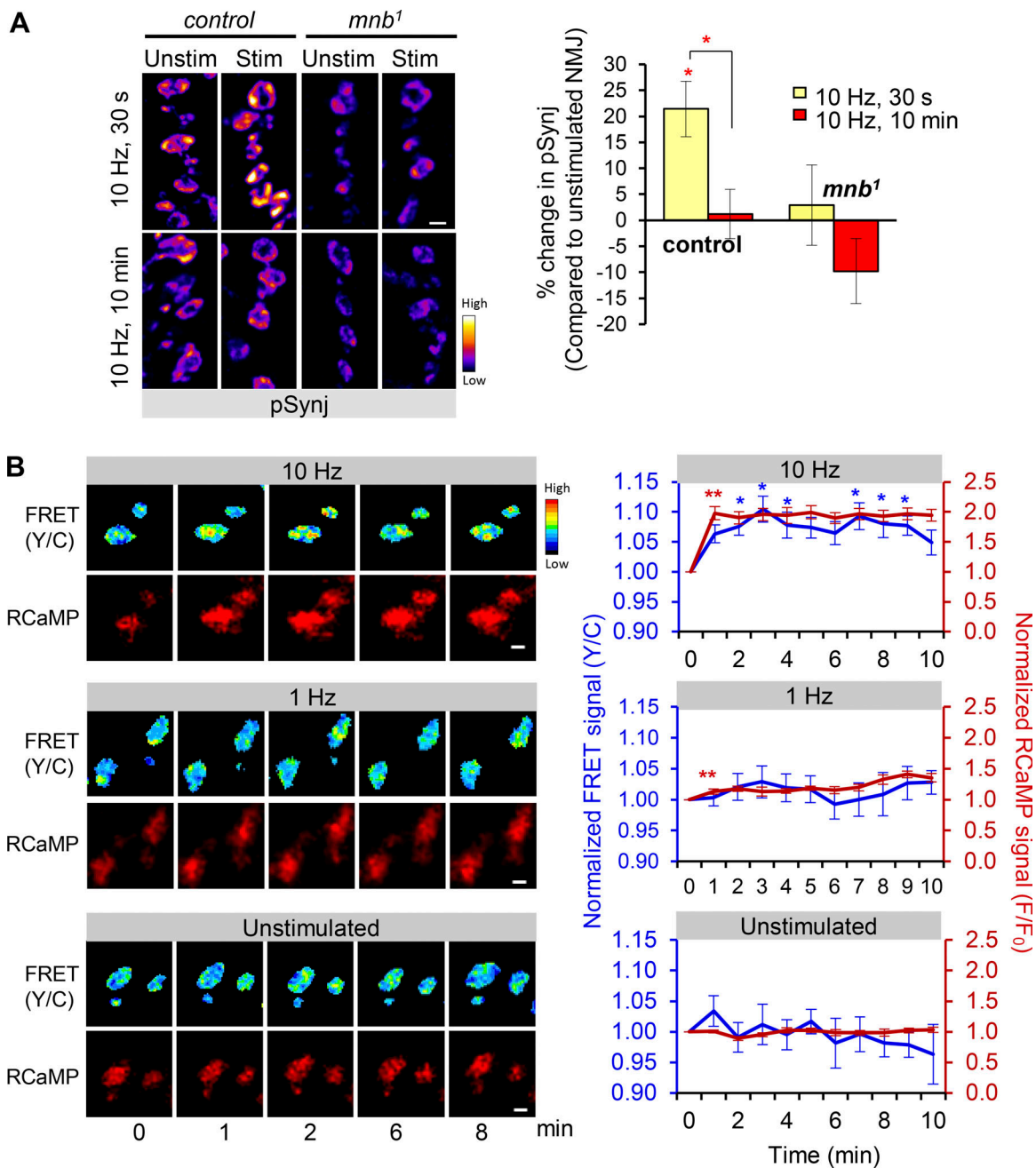
Figure 4. **Stimulation condition that induces ADBE is associated with reduced Synj phosphorylation by Mnb and increased CaN activation.** **(A)** Pseudo-colored images of NMJs stained with phospho-Synj antibody following stimulation (stim) at 10 Hz for 30 s or 10 min. Unstimulated (unstim) controls are NMJs with nerve in the suction electrode for the same period of time. Right graph shows percentage change in phospho-Synj level normalized to unstimulated NMJ of the same genotype. For 30-s protocol: control, $n = 14$; mnb^1, $n = 11$. For 10-min protocol: control, $n = 22$; mnb^1, $n = 13$. *, $P < 0.05$ compared with unstimulated control or as indicated. **(B)** Representative time-course images of NMJ expressing FRET-based CaN activity reporter, CaNAR2, and Ca^{2+} indicator RCaMP during indicated stimulations. Upper panel: Pseudo-colored images showing yellow/cyan ratio (Y/C). Graphs on the right show quantification of fold-change in CaN activity (calculated as Y/C emission ratio) and Ca^{2+} levels measured by RCaMP normalized to $t = 0$ (before stimulation). For unstimulated control, segmental nerve was placed into the suction electrode and was imaged using the same condition. $n = 12$ NMJ for 10 Hz, $n = 9$ for 1 Hz, and $n = 5$ for unstimulated. Scale bar = 2 µm for all figure panels. *, $P < 0.05$ compared with unstimulated control; **, $P < 0.05$ from that time point onward. All values represent mean ± SEM.

First, we assayed whether neuronal activity can further elevate $PI(4,5)P_2$ at the synapse by monitoring the level of $PLC_{\delta1}$-PH-eGFP, which binds to $PI(4,5)P_2$. Live imaging revealed that $PI(4,5)P_2$ in mnb^1 and $synj^{S1029A}$ can still increase along with neuronal activity (Fig. 6 A). Next, to address whether $PI(4,5)P_2$

elevation is required for ADBE, we took advantage of the ability of $PLC_{\delta1}$-PH-eGFP to shield and deplete $PI(4,5)P_2$ from interacting with endogenous binding partners, thereby blocking $PI(4,5)P_2$ signaling (Khuong et al., 2010). Dextran loading assay revealed that expression of $PLC_{\delta1}$-PH-eGFP alone reduced ADBE,

Peng et al.
Molecular mechanism coordinating endocytosis modes

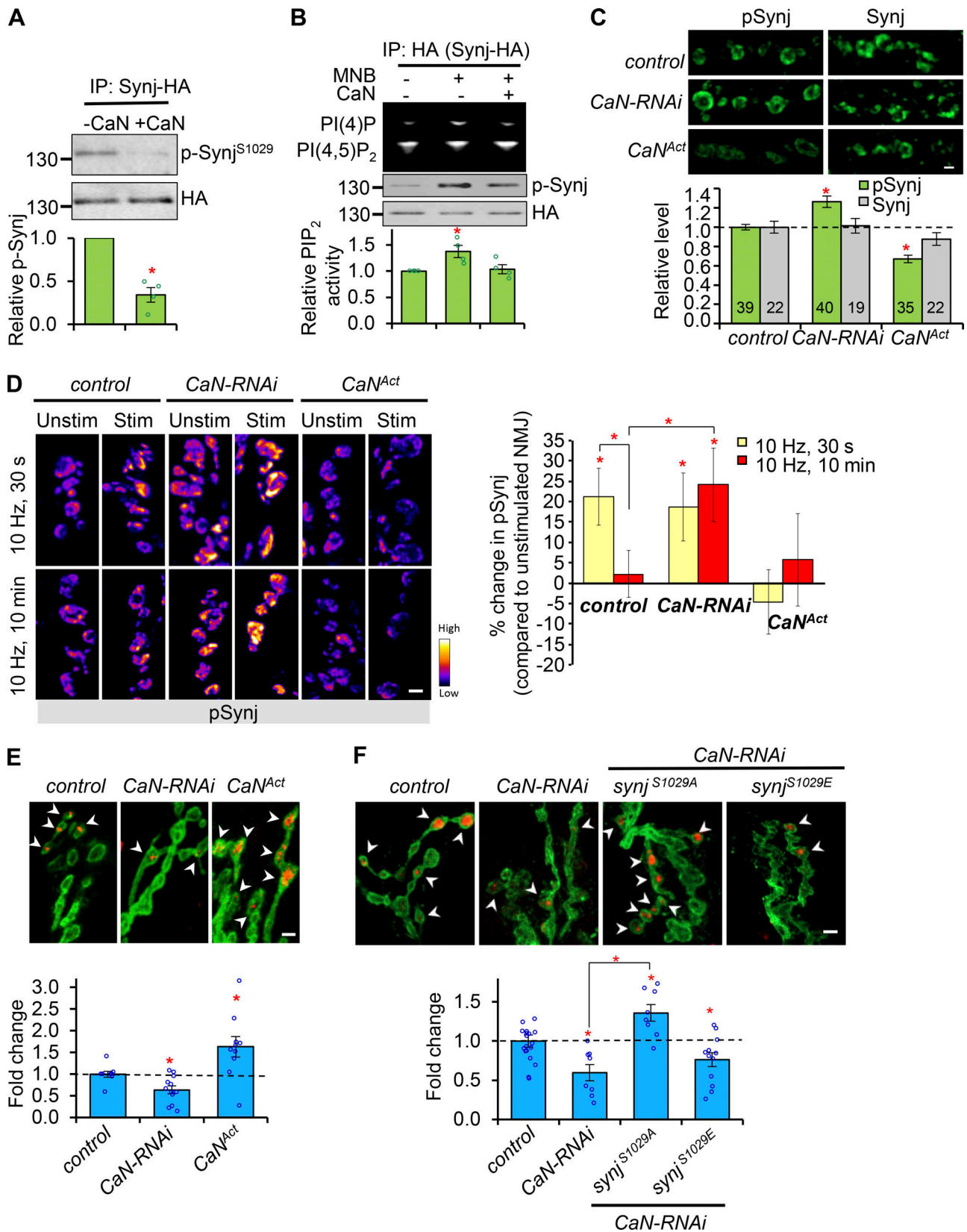Journal of Cell Biology   8 of 18
https://doi.org/10.1083/jcb.202011028

Figure 5. CaN dephosphorylates Synj at S1029 and is required for efficient ADBE. (A) Synj-HA was immunoprecipitated (IP) from fly heads and incubated with or without CaN. The level of Synj phosphorylated at S1029 was detected using p-Synj^{S1029} antibody and normalized to HA. $n = 4$ independent experiments. *, $P < 0.05$. **(B)** Top: TLC showing conversion of BODIPY-PI(4,5)P$_2$ to BODIPY-PI(4)P by Synj purified from fly heads with or without incubation with Mnb or CaN. Western blot represents levels of total Synj and phospho-Synj. Graph shows relative PI(4)P to PI(4,5)P$_2$ ratio normalized to the amount of Synj. $n = 4$ independent experiments. *, $P < 0.05$. **(C)** Basal levels of phospho-Synj and total Synj at the synapse. Number of NMJs examined is shown in the graph. *,

P < 0.05 compared with control. **(D)** Representative images of NMJ stained with p-Synj (pseudo-colored) after 10-Hz electrical stimulation (stim) for 30 s or 10 min. Unstimulated (unstim) controls are NMJs with nerve in the suction electrode for the same period of time. Percentage change in phospho-Synj level was normalized to unstimulated NMJ of the same genotype. For the 30-s protocol: control, $n = 12$; CaN-RNAi and CaN^{Act}, $n = 16$ per genotype. For 10-min stimulation: control, $n = 16$; CaN-RNAi and CaN^{Act}, $n = 15$ per genotype. *, P < 0.05 compared with unstimulated control or as indicated. **(E)** Dextran uptake assay reveals that perturbation in CaN alters ADBE. For control, $n = 9$; CaN-RNAi, $n = 12$; CaN^{Act}, $n = 10$. **(F)** Expression of $synj^{S1029A}$ bypasses the requirement for CaN in ADBE. For control, $n = 19$; CaN-RNAi, $n = 8$; CaN-RNAi background: $synj^{S1029A}$, $n = 8$; $synj^{S1029E}$, $n = 12$. For both E and F, NMJs are loaded with fluorescent-dextran (red) and stained with membrane marker HRP (green) following 10-Hz stimulation for 10 min. Fold-change was normalized to control. For C–F, scale bar = 2 µm. *, P < 0.05 compared with control or as indicated. Unless otherwise indicated, n values represent the number of NMJ assayed. All values represent mean ± SEM.

while blocking PI(4,5)P$_2$ signaling diminished dextran uptake in mnb^1 and $Synj^{S1029A}$ to the same level as PLC$_{\delta1}$-PH-eGFP (Fig. 6 B). These results are consistent with the dominant-negative effect of PLC$_{\delta1}$-PH-eGFP in blocking PI(4,5)P$_2$ signaling and further indicate that ADBE requires PI(4,5)P$_2$ elevation. Lastly, we tested

whether elevating PI(4,5)P$_2$ by up-regulating the level of phosphatidylinositol 4-phosphatase 5-kinase (PIP5K), which converts PI(4)P to PI(4,5)P$_2$ (van den Bout and Divecha, 2009), is sufficient to enhance ADBE. We found that neuronal expression of PIP5K increased synaptic PI(4,5)P$_2$ level and enhanced
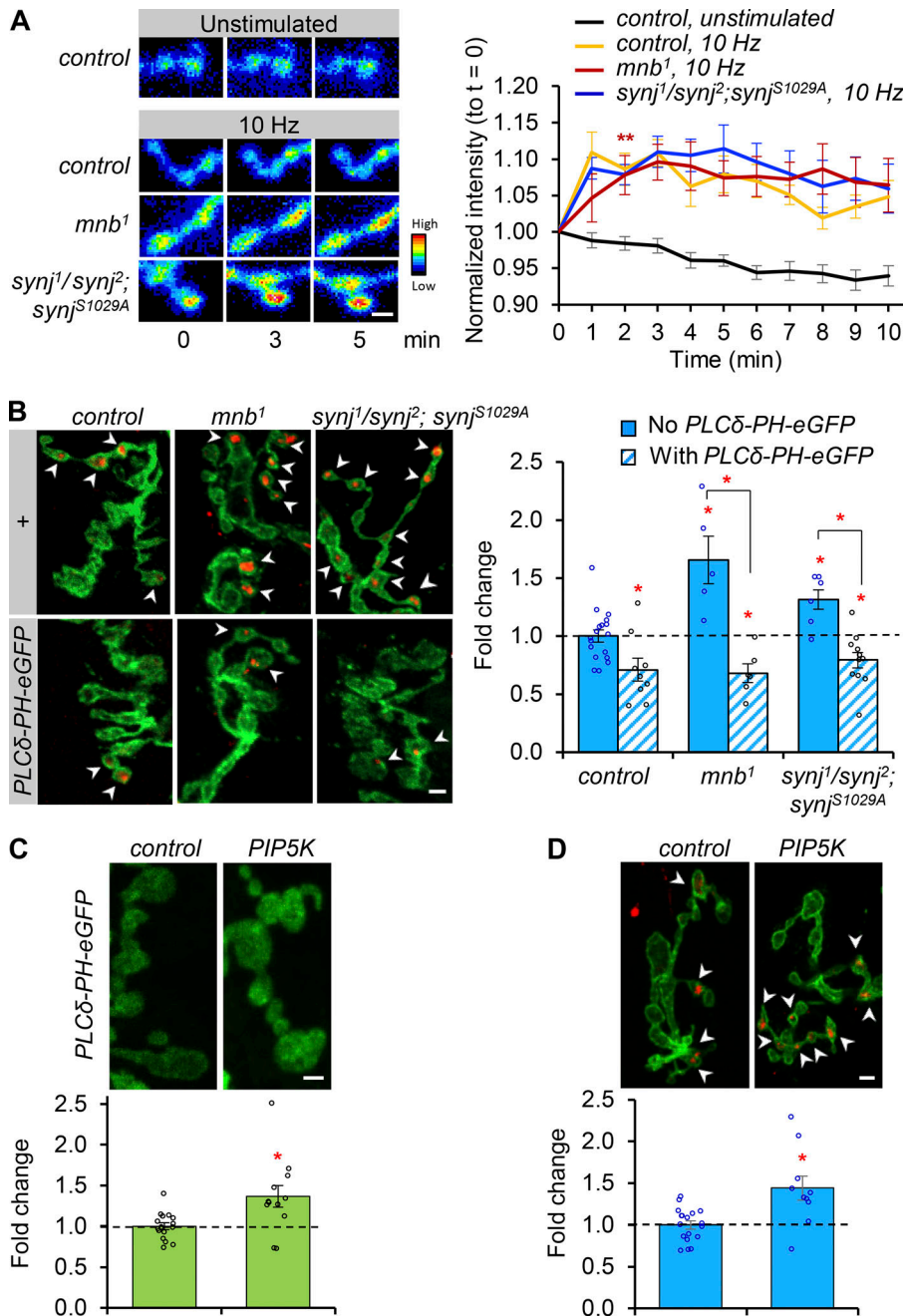

Figure 6. **PIP$_2$ content and Synj's dual phosphatase domains differentially regulate ADBE.** **(A)** Pseudo-colored time-course images of PLC$_{\delta1}$-PH-GFP signal during neuronal activity (left). Right graph shows change in PLC$_{\delta1}$-PH-GFP signal intensity normalized to $t = 0$ (before stimulation). For unstimulated control, segmental nerve was placed into the suction electrode and imaged using the same condition. $n = 12$ for unstimulated control, $n = 11$ for 10 Hz stimulated control, $n = 7$ for 10 Hz stimulated mnb^1, $n = 9$ for 10 Hz stimulated $synj^1/synj^2;synj^{S1029A}$. **, P < 0.05 from that time point onward. **(B)** Depletion of PIP$_2$ signaling by PLC$_{\delta1}$-PH-eGFP expression blocks ADBE. Representative images and quantifications of NMJ loaded with dextran (red) by 10-Hz stimulation for 10 min. HRP staining (green) was used to outline synaptic boutons (−PLC$_{\delta1}$-PH-GFP: control, $n = 18$, mnb^1, $n = 5$; $synj^{S1029}$ in synj mutant, $n = 6$. +PLC$_{\delta1}$-PH-GFP: control, $n = 9$, mnb^1, $n = 6$; $synj^{S1029}$ in synj mutant, $n = 11$). *, P < 0.05 compared with control NMJ without PLC$_{\delta1}$-PH-GFP or as indicated. **(C)** Neuronal overexpression of PIP5K elevates synaptic PI(4,5)P$_2$ level as detected by PLC$_{\delta1}$-PH-GFP signal intensity. For control, $n = 16$; for PIP5K OE, $n = 12$. **(D)** Images of NMJ loaded with dextran (red) and stained with HRP (green) following 10-Hz stimulation for 10 min. For control, $n = 18$; for PIP5K OE, $n = 10$. For C and D: *, P < 0.05 compared with control. Scale bar = 2 µm for all figure panels. n value indicates the number of NMJs examined. All values represent mean ± SEM.

dextran uptake (Fig. 6, C and D), confirming that high level of PI(4,5)P$_2$ promotes ADBE.

Although high PI(4,5)P$_2$ content is a requirement for ADBE, the finding that synj^1/synj^2 has reduced ADBE while displaying elevated PI(4,5)P$_2$ further suggests that PI(4,5)P$_2$ elevation is not sufficient, and Synj likely regulates ADBE through its distinct functional domains. We generated transgenic flies with defects in each of Synj's functional domains (Fig. 7 A): (1) 5′-PPase deficient, Synj$^{5'-AD}$; (2) SAC1 activity deficient, Synj^{SAC-AD}; and (3) Synj with the proline rich domain (PRD) truncated, Synj^{ΔPRD}, so that it cannot bind to other known endocytic proteins such as endophilin and Dap160 (McPherson et al., 1996; Cremona and De Camilli, 1997; Schuske et al., 2003; Verstreken et al., 2003; Mani et al., 2007; Dong et al., 2015). Western blot analyses indicated that Synj^{ΔPRD} likely renders the protein unstable, since the level of Synj^{ΔPRD} protein is reduced in all the synj^{ΔPRD} flies tested (Fig. S4 B). We confirmed that Synj$^{5'-AD}$ and Synj^{SAC-AD} indeed blocked 5′-PPase and SAC1 activity, respectively (Fig. S4, C and D), and that Synj^{ΔPRD} does not interact with endophilin (Fig. S4 E). Next, we monitored the ability of Synj functional mutants to affect CME. Expression of synj$^{5'-AD}$ in synj mutant background failed to rescue reduced FM1-43 loading stimulated using the CME protocol, whereas either Synj^{SAC-AD} or synj^{ΔPRD} effectively restored FM1-43 load (Fig. S5, A and B). FM1-43 unloading experiments confirmed that the decreased dye uptake in synj$^{5'-AD}$ is indeed due to a defect in endocytosis and not exocytosis (Fig. S5 C). These results indicate that Synj's 5′-PPase activity, or the ability to convert PI(4,5)P$_2$ to PI(4)P, is essential for CME, but SAC1 and PRD domains of Synj are dispensable for CME at the *Drosophila* NMJ.

Next, we examined which of Synj's functional domains is crucial for ADBE by measuring the dextran uptake index during intense neuronal stimulation. Interestingly, expression of synj$^{5'-AD}$ in synj mutant enhanced dextran uptake above wild-type synapses, suggesting that Synj's ability to convert PI(4,5)P$_2$ to PI(4)P suppresses ADBE. Expression of synj^{SAC-AD} in synj mutant, on the other hand, failed to restore dextran uptake, revealing an unexpected requirement for SAC1 activity in ADBE (Fig. 7, B and C). As SAC1 domain of Synj could potentially affect Synj targeting (Dong et al., 2015), we examined Synj mutant protein distribution at the synapse. Immunostaining revealed that the level of Synj^{SAC-AD} at the synapse is comparable to the Synj^{WT} construct, further indicating that defective ADBE is due to decreased SAC1 activity and not a change in Synj distribution (Fig. S5 D). Recent reports demonstrated that a mutation in the SAC1 domain of Synj (Synj$^{SAC-R258Q}$), which blocks Synj's SAC1 activity while leaving the 5′-PPase activity intact (Fig. S4, C and D), causes Parkinson's disease (PD; Krebs et al., 2013). We therefore investigated the effect of this PD-causing mutation in modulating ADBE. synj$^{SAC-R258Q}$ expression in synj mutant also failed to restore dextran uptake during intense neuronal activity, further strengthening the claim that Synj's SAC1 activity is required for efficient ADBE (Fig. 6 C). Lastly, we tested the importance of Synj–endophilin interaction in modulating ADBE. Despite having a lower level of Synj^{ΔPRD} at the synapse (Fig. S5 D), it is sufficient to rescue the dextran uptake index in synj mutant to control levels, suggesting that the PRD domain of Synj is dispensable for

ADBE. Together, these findings indicate that Synj's regulation of phosphoinositide content through its dual phosphatase domain plays distinct roles in modulating ADBE: the 5′-PPase activity of Synj suppresses ADBE, while Synj's SAC1 activity is required for ADBE.

Lastly, we assessed the interplay between phosphorylation of Synj at S1029, 5′-PPase, and SAC1 activities in regulating ADBE. Given that synj^{SAC-AD} display defective ADBE, we tested whether inhibiting Synj S1029 phosphorylation, which leads to reduced 5′-PPase activity (Geng et al., 2016), is sufficient to restore ADBE in synj^{SAC-AD}. Because mnb and synj double mutants are lethal (Geng et al., 2016), we blocked Mnb-dependent phosphorylation of Synj at S1029 using proINDY (Chen et al., 2014). Fig. 7 D shows that proINDY treatment enhanced dextran uptake in synj mutants expressing synj^{WT} but not in synj^{S1029A} flies, further confirming that dephosphorylation of Synj promotes ADBE during neuronal activity. On the other hand, proINDY treatment did not rescue ADBE in synj^{SAC-AD}, suggesting that SAC1 activity is required for reliable ADBE even when Synj is dephosphorylated.

Discussion

Synapses use multiple modes of SV retrieval to optimize neurotransmission. Despite the identification of ADBE many decades ago (Miller and Heuser, 1984), molecular mechanisms underlying ADBE remain ill defined, and how neurons coordinate different modes of endocytosis to prevent depletion of SVs during neuronal activity remains an unanswered question. Data presented in this paper identify Mnb and Synj as novel proteins modulating ADBE at the *Drosophila* NMJ and further unveil that coordinated activations of CME and ADBE during neuronal activity require dynamic regulation of Synj function by Mnb and CaN (Fig. 7 E).

Different modes of endocytosis

There are at least four proposed modes of SV retrieval used by neurons during different stimuli: CME, kiss-and-run, ultrafast endocytosis, and ADBE. Except for CME, the proposed retrieval modes do not require clathrin for endocytosis (Kononenko and Haucke, 2015; Gan and Watanabe, 2018; Chanaday et al., 2019). Several studies have established that Mnb and Synj are essential for efficient CME (Cremona et al., 1999; Verstreken et al., 2003; Chen et al., 2014; Geng et al., 2016), and Synj has been implicated in CIE (Mani et al., 2007). In this paper, we further demonstrate novel functions of Mnb and Synj in regulating clathrin-independent ADBE. One challenge in studying ADBE has been difficulty in distinguishing ADBE from other endocytosis modes. Here, FM1-43 and dextran dye loading strategies, coupled with stimulation conditions known to correlate with different SV retrieval modes, were used to examine ADBE. First, by monitoring FM1-43 dye uptake while pharmacologically or genetically blocking clathrin function, we demonstrated that Mnb and Synj have divergent roles in CIE, with Mnb acting as a suppressor and Synj as essential for efficient CIE. Next, to further distinguish subtypes of CIE affected, we labeled the NMJ with dextran following electrical stimulation at different frequencies and duration. Although the size of 10-kD fluorescent dextran is
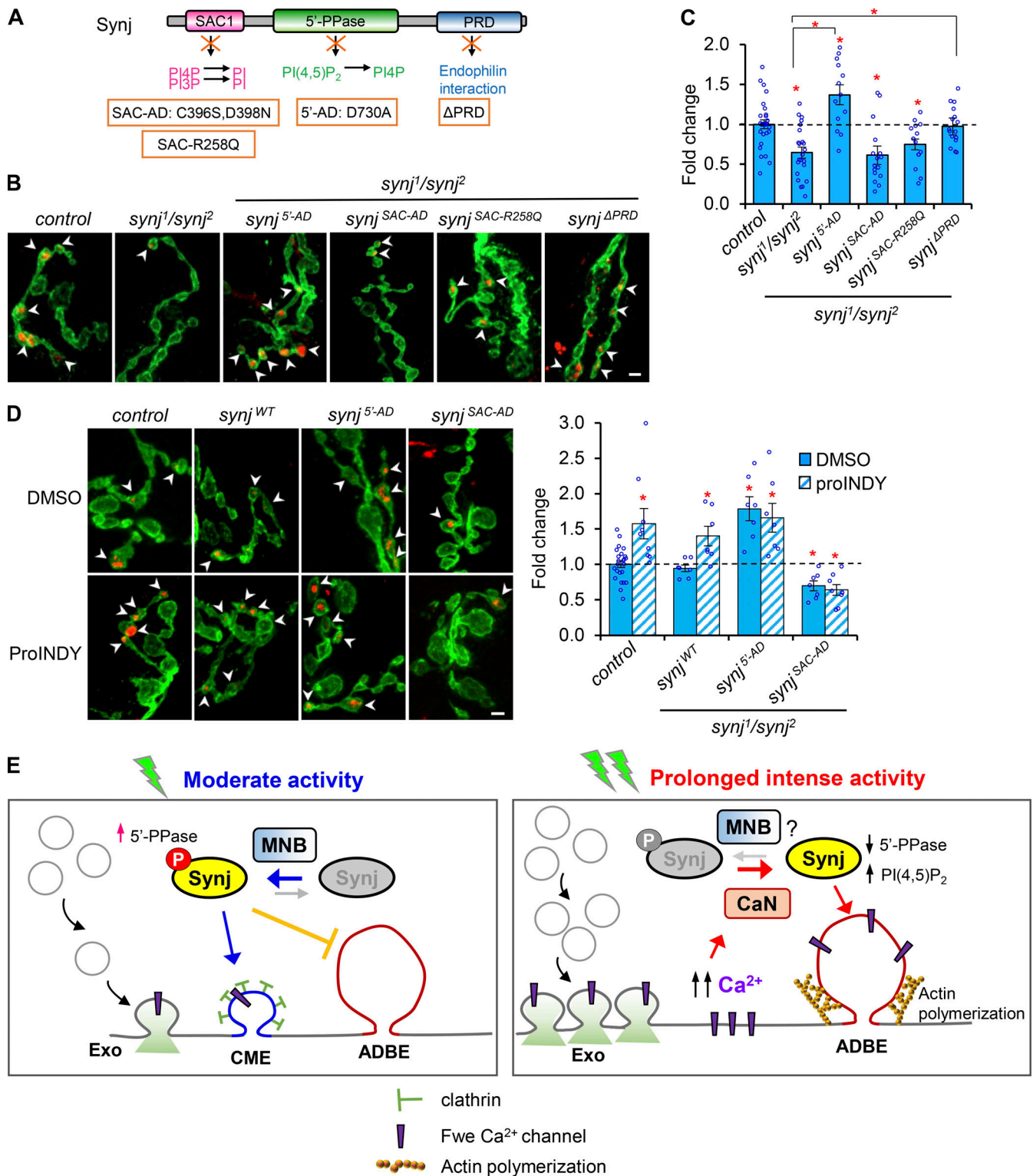
Figure 7. **Synj's 5'-PPase suppresses ADBE, while its SAC activity is required for normal ADBE. (A)** Schematic of Synj domains and their known functions. Synj functional domain mutants are highlighted by orange boxes. **(B)** Images of NMJ loaded with dextran (red) and stained with HRP (green) following 10-Hz stimulation for 10 min. **(C)** Fold change in dextran uptake. For control, $n = 30$; synj mutant, $n = 28$. In synj mutant background: synj[5'-AD], $n = 13$, synj[SAC-AD], $n = 16$; synj[SAC-R258Q], $n = 14$; synj[ΔPRD], $n = 16$. *, $P < 0.05$ compared with control. **(D)** Acute inhibition of Mnb by proINDY enhances dextran uptake in Synj[WT] but not in flies with deficient SAC domain. For DMSO treatment: control, $n = 25$. In synj mutant background: synj[WT], $n = 7$; synj[5'-AD], $n = 7$; synj[SAC-AD], $n = 7$. For proINDY treatment: control, $n = 9$. In synj mutant background: synj[WT], $n = 7$; synj[5'-AD], $n = 7$; synj[SAC-AD], $n = 8$. In B and D, scale bar = 2 µm. n value indicates the number of NMJs examined. All values represent mean ± SEM. **(E)** Model depicting Mnb- and CaN-dependent coordination of endocytosis modes through phosphorylation of Synj. Mnb phosphorylates Synj to enhance Synj's 5'-PPase activity, thereby facilitating CME but suppressing ADBE during moderate activity. During prolonged intense activity, higher intracellular Ca^{2+} activates CaN, which further dephosphorylates Synj to promote ADBE. This may or may not be coupled with Mnb inactivation during prolonged activity. Dephosphorylation of Synj reduces its 5'-PPase activity, and ADBE is enhanced through $PI(4,5)P_2$ accumulation and actin polymerization. Normal ADBE also requires Synj's SAC domain (not depicted).

theoretically small enough to be taken up by single SVs, the low concentration of dextran used and the fact that it does not preferentially bind to membrane make it unlikely to label single-vesicle retrieval such as CME and kiss-and-run with high efficiency (Clayton and Cousin, 2009a). Consistent with this, 1-Hz stimulation did not elevate dextran uptake above unstimulated control. Furthermore, although both ultrafast endocytosis and ADBE retrieve membrane larger than the size of a single SV, ultrafast endocytosis can be triggered by mild stimulation or even single action potentials (Watanabe et al., 2013a; Watanabe et al., 2013b; Delvendahl et al., 2016), while ADBE is selectively activated by prolonged intense neuronal activity. Our finding that only prolonged strong stimulation (10 Hz for 10 min) resulted in dextran uptake above background thus indicates that the dextran uptake assay is selectively labeling ADBE. Note that we did not use pHlourin proteins to monitor ADBE, mainly because commonly used synaptic pHlourin proteins are sorted through CME (Nicholson-Fish et al., 2015), and the newly identified molecular cargo for ADBE, VAMP4, is not conserved in *Drosophila*. Taken together, by using different dye labeling and stimulation strategies, coupled with TEM, we demonstrate that Mnb suppresses ADBE while Synj is necessary for ADBE.

Molecular mechanisms required for ADBE

Our data demonstrate that dephosphorylation of Synj by CaN is a molecular switch that activates ADBE at the *Drosophila* NMJ. We showed that prolonged stimulation triggered dephosphorylation of Synj (Fig. 4 A) and enhanced CaN activity (Fig. 4 B). We also demonstrated that Synj is a substrate of CaN in vitro and in vivo (Fig. 5, A–C). CaN has been shown to dephosphorylate various endocytic proteins (Cousin and Robinson, 2001), and is universally required for all modes of endocytosis (Wu et al., 2014a). In line with this, knockdown of CaN using RNAi significantly diminished ADBE (Fig. 5 E). Importantly, expression of dephosphorylated Synj but not phosphorylated Synj bypassed the requirement for CaN in ADBE (Fig. 5 F). While our data do not exclude the involvement of other substrates of CaN in regulating ADBE, these findings reveal that dephosphorylation of Synj by CaN is a key step in ADBE.

Another prerequisite for ADBE is local $PI(4,5)P_2$ elevation. Using Synj functional domain mutants, we found that Synj's 5′-PPase is essential for CME but negatively regulates ADBE (Fig. 7 C). The role of the 5′-PPase domain in CME is consistent with previous reports (Mani et al., 2007). Negative regulation of ADBE by Synj's 5′-PPase is likely due to its removal of $PI(4,5)P_2$, since $PI(4,5)P_2$ accumulation favors actin polymerization, which propels membrane inward for ADBE (Holt et al., 2003; Richards et al., 2004; Gormal et al., 2015; Wu et al., 2016; Soykan et al., 2017). Furthermore, consistent with a report that showed local $PI(4,5)P_2$ elevation during intense neuronal activity is necessary for ADBE (Li et al., 2020), depleting $PI(4,5)P_2$ signaling effectively abolished the enhanced ADBE phenotype seen in *mnb[1]* or phospho-null *synj[S1029A]* (Fig. 6 B). Up-regulating the levels of $PI(4,5)P_2$ by expression of PIP5K in neurons also enhanced ADBE (Fig. 6 D). Together, these data indicate that local $PI(4,5)P_2$ elevation promotes ADBE.

One other requirement for normal ADBE involves Synj's SAC1 activity, although how it regulates ADBE is unclear. One

plausible explanation is that SAC1 has other functions such as targeting Synj to the synapse (Dong et al., 2015). However, we found that point mutations that abolish SAC1 activity (Synj[SAC-AD] and the PD-causing mutation Synj[SAC-R258Q]) did not alter Synj localization to the synapse (Fig. S5 D). Synj's SAC1 activity converts PI(4)P, PI(3)P, or PI(3,5)P to PI, with PI(4)P as its preferred substrate in vivo (Guo et al., 1999). Loss of SAC1 activity could therefore lead to local accumulation of these phosphoinositides to alter membrane identity or downstream signaling pathways required for ADBE. There is evidence that PI(4)P deforms lipid membrane into tighter curvature (Furse et al., 2012; Furse et al., 2016), implying that the presence of PI(4)P would favor single-vesicle conformation (tighter curvature) and prevent large bulk invagination (shallower curvature). Future experiments examining the role of SAC1 phospholipid substrates and their binding proteins in modulating endocytosis will shed light on molecular mechanisms controlling ADBE. Interestingly, the PD-causing Synj[SAC-R258Q] mutation has also been shown to block autophagy and slow the rate of CME (Cao et al., 2017; Vanhauwaert et al., 2017). Although we find that Synj's SAC1 activity is not required for overall CME, which was reported by Cao et al. (2017), we do not exclude the possibility that it could potentially alter endocytosis efficiency. Currently, the connection between different endocytosis modes and autophagy is not known, and it will be interesting to investigate the relationship between bulk endocytosis and autophagy pathways in maintaining synaptic functions in the future.

Synj also contains a PRD required for interaction with SH3 domain proteins. Our work revealed that Synj's function in ADBE at the *Drosophila* NMJ does not rely on its PRD. We found that Synj[ΔPRD] still localized to the synapse, albeit at a lower level (Figs. S4 B and S5 D). Nevertheless, Synj[ΔPRD] still rescued ADBE in *synj* mutant. Curiously, Mnb- and CaN-dependent modulations of Synj phosphorylation at S1029 is located in the PRD domain, raising the question of why Synj[ΔPRD] rescues defective ADBE in *synj* mutant while phosphomimetic Synj[S1029E] could not. We speculate this may be due to the presence of a low amount of synaptic Synj[ΔPRD] with normal 5′-PPase and SAC1 activities. This will likely result in reduced $PI(4,5)P_2$ turnover rate while Synj[ΔPRD] retains sufficient SAC1 activity to allow ADBE to occur during intense stimulation. Taken together, we propose that $PI(4,5)P_2$ elevation together with removal of phosphoinositides by Synj's SAC1 domain is essential for the completion of ADBE.

Coordination of CME and ADBE during neuronal activity

How do Mnb, Synj, and CaN integrate different stimulus strength to maintain efficient endocytosis at the *Drosophila* NMJ? We envision the following scenario (Fig. 7). During mild neuronal activity, transient increase in local $PI(4,5)P_2$ level at the plasma membrane is known to recruit adaptor proteins, clathrin, and various endocytic proteins and initiate actin polymerization, all of which are necessary for CME (Wenk and De Camilli, 2004; Haucke, 2005). Subsequent conversion of $PI(4,5)P_2$ to PI(4)P by Synj's 5′-PPase domain results in uncoating of clathrin and termination of actin polymerization. During moderate activity or short-term intense stimulation, enhanced phosphorylation of Synj by Mnb further boosts Synj's

5′-PPase activity (Geng et al., 2016; Fig. 5 B). We speculate that this acute increase in Synj's 5′-PPase activity allows neurons to adapt to increased synaptic demand by augmenting the efficiency of $PI(4,5)P_2$ removal and uncoating of clathrin, thereby facilitating CME. Furthermore, as ADBE depends on actin polymerization for membrane internalization, the rapid drop in $PI(4,5)P_2$ terminates actin polymerization, thereby preventing the uptake of large membrane areas and suppressing ADBE. With continued intense neuronal activity, increased Ca^{2+} due to translocation of the Fwe Ca^{2+} channel from the SV membrane to the periactive zone likely augments CaN phosphatase activity (Yao et al., 2017; Li et al., 2020), resulting in CaN-dependent dephosphorylation of Synj (which may or may not be coupled with Mnb inactivation during prolonged stimulation). Dephosphorylated Synj has reduced 5′-PPase activity (Geng et al., 2016), thereby delaying $PI(4,5)P_2$ turnover at the periactive zone. Positive regulation of $PI(4,5)P_2$ on Fwe channel activity likely prolongs suppression of Synj's 5′-PPase activity to enhance local $PI(4,5)P_2$ accumulation, promote actin polymerization, and initiate bulk membrane invagination at the periactive zone. Synj's SAC1 activity then removes its phosphoinositide substrates necessary for bulk endocytosis (Fig. 7 E). Together, temporal regulation of Synj's phosphorylation status and PPase activity by Mnb and CaN enable neurons to respond by tuning endocytosis modes based on synaptic demand.

The ability to maintain reliable synaptic transmission across a dynamic range of neural activity is essential for normal neuronal function, and synaptic dysfunctions have been implicated in a large number of neurologic disorders (Li and Kavalali, 2017; Bonnycastle et al., 2021). Intriguingly, Mnb and Synj have been linked to multiple neurologic disorders: both Mnb and Synj are up-regulated in Down's syndrome (Guimera et al., 1999; Arai et al., 2002), Mnb is a strong candidate gene for autism (Iossifov et al., 2012; O'Roak et al., 2012), and Synj is mutated in PD (Krebs et al., 2013). There are also reports of increased incidence of PD in adults with autism (Starkstein et al., 2015). Using *Drosophila* as a model system, this work provides important insights into Mnb and Synj functions in coordinating multiple modes of endocytosis. Future studies examining Mnb and Synj interactions in regulating SV endocytosis modes in the mammalian system will have important implications for understanding neurologic disorders. It will also be important in the future to further investigate mechanisms regulating Mnb kinase activity during neuronal activity, roles of different phosphoinositides in distinct modes of endocytosis, and the function of Mnb in regulating SV reformation.

Materials and methods

Fly stock

Flies were grown on standard cornmeal, yeast, sugar, and agar medium at 25°C under a 12-h dark/light cycle. White-eyed flies (w^{1118}) crossed to the driver were used as wild-type control throughout all experiments. The following fly lines were used: mnb^1 (from Dr. Martin Heisenberg, University of Wurzburg, Wurzburg, Germany), $synj^1$ and $synj^2$ (from Dr. Hugo Bellen, Baylor College of Medicine, Houston, TX), *UAS-CaNB-RNAi*

(Bloomington Drosophila Stock Center [BDSC]; 27307], *UAS-RCaMP* (BDSC; 63792), *UAS-PLCδ1-PH-eGFP* (BDSC; 39693), *UAS-hPIP5K* (BDSC; 86256), and *UAS-lap-RNAi* (BDSC; 39021). *UAS-mnb*, *UAS-synj^{wt}*, *UAS-synj^{S1029A}* and *UAS-synj^{S1029E}* were described previously (Chen et al., 2014; Geng et al., 2016), and *UAS-CaN^{act}* was generated previously (Shaw and Chang, 2013). *UAS-cyto-CaNAR2* was generated by cloning cyto-CaNAR2 (Addgene; plasmid 64729) into KpnI/XbaI sites of pUASTattB vector. Synj domain mutant transgene constructs were generated by site-directed mutagenesis and subcloned into the pINDY6 vector containing a HA tag. To drive neuronal expression, *Elav-Gal4* (BDSC; 458) and n-synaptobrevin-Gal4 (*nSyb-Gal4*; Pauli et al., 2008; kindly provided by Dr. Julie Simpson, University of California, Santa Barbara, Santa Barbara, CA) were used as indicated. All other stocks and standard balancers were obtained from Bloomington Stock Center.

Immunochemistry

Third-instar larvae were dissected in Ca^{2+}-free dissection buffer (128 mM NaCl, 2 mM KCl, 4.1 mM $MgCl_2$, 35.5 mM sucrose, 5 mM Hepes, and 1 mM EGTA) and fixed with 4% PFA for 25 min at RT. Fixed samples were washed with PBS containing 0.1% Triton X-100 (PBST), blocked with 5% normal goat serum in PBST, and incubated overnight in primary antibody at 4°C. Preparations then were washed with PBST, incubated in secondary antibody for 1 h at RT, washed, and mounted. The following primary antibodies were used: rabbit anti-Synj-1, 1:200 (Chen et al., 2014); rabbit anti-p-Synj (from Dr. Hugo Bellen), 1:1,000; rabbit anti-p-Synj^{S1029} (Geng et al., 2016), 1:200; and Alexa Fluor 488– or Cy3-conjugated anti-HRP, 1:100 (Jackson ImmunoResearch Laboratories). Secondary antibodies used were Alexa Fluor 488 or 555 conjugated, 1:250 (Invitrogen).

Images of synaptic terminals from NMJ 6/7 in A2 or A3 segments were captured using Zeiss LSM800 confocal microscope 63×, 1.4 numerical aperture oil-immersion objective with a 0.7× or 1× zoom. Staining intensities were calculated by normalizing the fluorescence intensity to the bouton area outlined by HRP staining. When comparing intensity across genotypes, imaging acquisition parameters were kept constant, and all values were normalized to the control done within the same experimental set.

For electrical stimulation experiments, third-instar larvae were dissected in Ca^{2+}-free HL-3 (70 mm NaCl, 5 mm KCl, 20 mM $MgCl_2$, 10 mM $NaHCO_3$, 5 mM Trehalose, 115 mM sucrose, 5 mM Hepes, and 2.5 mM EGTA, pH 7.2). A3 segmental motor nerves were stimulated using a suction electrode in 2 mM Ca^{2+} HL-3 at indicated frequency and duration. For unstimulated control, nerves were sucked into the electrode, but no electrical stimulation was applied. Samples were then fixed immediately with 4% PFA after stimulation, followed by staining procedures as described above. Muscle 6/7, A3 were imaged.

FM 1-43 labeling

Third-instar larvae were dissected in Ca^{2+}-free HL-3 solution. For CME loading experiments, dissected samples were stimulated with modified HL-3 containing 90 mM K^+/ 0.5 mM Ca^{2+} (Verstreken et al., 2008; Yao et al., 2017; 25 mM NaCl, 90 mM

KCl, 10 mM MgCl$_2$, 10 mM NaHCO$_3$, 5 mM trehalose, 5 mM Hepes, 30 mM sucrose, and 0.5 mM CaCl$_2$) in the presence of 4 μM FM 1-43 (Invitrogen) for 1 min, and then washed with Ca^{2+}-free HL-3 solution to remove excess dye. For unloading experiments, larvae were stimulated with 90 mM K$^+$/0.5 mM Ca^{2+} solution for 30 s to unload FM1-43 dye. Synaptic boutons in muscle 6/7 in A2 or A3 segments were taken using Zeiss LSM800 confocal microscope with a 40× water-dipping objective. Fluorescence intensities were measured using ImageJ. The unloading efficiency was calculated as (F_{loaded} − F_{unload})/F_{loaded}. All genotypes were normalized to control done within the same experimental set.

For CPZ treatment, third-instar larvae were dissected in Ca^{2+}-free HL-3 solution with the brain intact and incubated with 50 μM CPZ in Schneider's medium (Thermo Fisher Scientific) for 30 min at RT. Subsequently, larval brain was removed and the NMJ was loaded with 4 μM FM 1-43 by using 60 mM K$^+$/2 mM Ca^{2+} stimulation for 10 min in the presence of 50 μM CPZ (CIE protocol). ImageJ was used to measure intensity normalized to bouton area. To calculate membrane inclusion area following CIE protocol, synaptic boutons with punctate staining were circled manually in ImageJ, and the inclusion area was normalized to bouton area. FM1-43 staining was considered punctate when the dye appeared as bright spots or clusters located near the central portion of the bouton (not uniform peripheral staining seen for CME protocol). Due to the small size of the type Is boutons, only type Ib were analyzed. Note that because the resolution of FM1-43 staining in live confocal images is not sufficient to distinguish a single invaginated membrane structure, the area of inclusion reflects the extend of bulk endocytosis rather than the number or the size of bulk endosomes. To calculate the number of boutons with inclusions, boutons with punctate staining were counted and normalized to the total number of boutons. To minimize bias, samples were blinded so that the experimenter did not know the genotype/condition of the samples during analysis.

Dextran dye labeling

Third-instar larvae were dissected in Ca^{2+}-free HL-3 solution with the brain intact, incubated with 1 mg/ml type IV collagenase for 30 s in Ca^{2+}-free HL-3 solution, and then washed. The brain was then removed by cutting the segmental nerves close to the brain, and the A3 segmental nerve was electrically stimulated in HL-3 solution containing 2 mM CaCl$_2$ and 100 μM tetramethylrhodamine-dextran dye (Thermo Fisher Scientific; D1816). Larvae were then washed with Ca^{2+}-free HL-3 for 2 min to remove excess dextran and fixed with 4% PFA for 30 min at RT. Presynaptic boutons were labeled by Alexa Fluor 488–conjugated anti-HRP, and dextran loading was examined using a Zeiss LSM800. The dextran load index was determined by counting the number of labeled boutons in muscle 6/7 of A3, divided by the total number of HRP-labeled boutons in each NMJ. Fold-change in dextran uptake index was calculated and presented in the graphs. Note that there were some day-to-day variations in the dextran uptake index for the stimulated control (ranging from 0.25 to 0.50), but the test genotypes always followed the same trend as the control (i.e., if the control had a

higher dextran uptake index that day, mnb^1 trended even higher that day). This variation is likely due to differences in daily optimized imaging parameters, subtle differences in daily collagenase enzyme or dextran dye preparations, and treatment by different experimenters. Due to the number of genotypes, it was not possible to examine all genotypes in parallel on the same day each time. Thus, to minimize bias and to obtain reliable measurement of ADBE across all genotypes, dextran uptake index values were always normalized to the control NMJs done in parallel within the same experimental set, and fold-changes were presented in the graph.

For proINDY drug treatment, dissected larvae were preincubated in Schneider's medium containing 0.2% DMSO (vehicle control) or 50 μM proINDY for 30 min, as described previously, before dextran labeling (Chen et al., 2014). proINDY or 0.2% DMSO (vehicle control) was also included during stimulation.

EM

Third-instar larvae were dissected in Ca^{2+}-free HL-3 solution, and A3 segmental motor nerve was electrically stimulated in 2 mM Ca^{2+} HL-3 at 10 Hz for 10 min. For CME and CIE protocols, NMJs were stimulated using high KCl as indicated above. Following stimulation, samples were immediately fixed with freshly prepared 4% PFA and 1% glutaraldehyde in 1 mM MgCl$_2$, 1 mM EGTA, and 0.1 M Na-cacodylate buffer, pH 7.2, for 30 min at RT and then overnight at 4°C. Stimulated muscle segments (muscle 6/7, A3) were then trimmed and subsequently stored in 4% PFA in PBS at 4°C until further processing. Muscle segments were then washed three times in distilled water and poststained in 1% osmium tetroxide in distilled water for 60 min at RT and in ferrocyanide-reduced osmium tetroxide for 30 min. After washing three times in distilled water, segments were dehydrated in a graded acetone series and infiltrated with 25% uncatalyzed Spurr's resin in acetone for 24 h and 50% uncatalyzed Spurr's resin in acetone for 24 h, followed by two 24-h changes of 100% uncatalyzed Spurr's and polymerization in freshly catalyzed Spurr's for 24 h at 60°C. 60-nm-thin sections were collected on Formvar-coated 2 × 1-mm slot grids, stained with 2% uranyl acetate and Reynolds lead citrate, and imaged by TEM at 80 kV in a Zeiss EM10 (Carl Zeiss Microscopy) equipped with an Erlangshen charge-coupled device camera (Gatan).

Cyto-CaNAR2 FRET imaging

The CaN FRET biosensor, cyto-CaNAR2 (Mehta et al., 2014), was expressed by neuronal Elav-Gal4 driver to measure synaptic CaN activity. Third-instar larvae were dissected in Ca^{2+}-free HL-3 solution and then electrically stimulated in 2 mM Ca^{2+} HL-3 solution. Images were captured before and during stimulation at indicated time points using an Olympus FV3000RS confocal microscope with a 40× water-dipping objective. The YFP and CFP intensities were imaged using excitation at 405 nm and detection wavelengths 430–490 nm for CFP and 515–550 nm for YFP. RCaMP signal was imaged using excitation at 561 nm and detection wavelengths 580–670 nm. Fluorescence intensities were corrected by subtracting background using ImageJ, and the emission ratio (YFP/CFP) was calculated at each time point. All

time courses were normalized to the emission ratio before stimulation. For FK506 treatment, NMJs were incubated with either DMSO as vehicle control or 10 μM FK506 in 2 mM Ca^{2+} HL-3 solution for 30 min before 10-Hz stimulation for 10 min.

PI(4,5)P$_2$ imaging
PLCδ1-PH-eGFP expressed by nSyb-gal4 driver was used to measure the levels of PI(4,5)P$_2$. Third-instar larvae were dissected in Ca^{2+}-free HL-3 solution. For fixed images, dissected samples with brain intact were fixed with 4% PFA for 30 min, washed with PBST, and then incubated with Cy3-HRP for 30 min. PLCδ-PH-eGFP intensity was analyzed by outlining the bouton area using HRP in ImageJ and normalized to the control within the same experimental set. For live imaging, dissected samples were electrically stimulated at 10 Hz for 10 min in 2 mM Ca^{2+} HL-3 solution. Images were taken before and at indicated time points during stimulation. PLCδ1-PH-eGFP intensity of the same boutons at each time point were measured and corrected by subtracting background using ImageJ. All time courses were normalized to the before-stimulation intensity.

In vitro dephosphorylation of Synj by CaN
Approximately 100 fly heads expressing HA-Synj were homogenized in lysis buffer (10 mM Hepes, 100 mM NaCl, 10 mM EDTA, 1% NP-40, 1 mM Na$_3$VO$_4$, 50 mM NaF, 250 nM cyclosporin A, and protease inhibitor) and centrifuged to removed debris. Extracts were then incubated and rotated with 20 μl anti-HA-Agarose (Sigma-Aldrich) overnight at 4°C to pull down Synj. Unbound proteins were removed by washes with lysis buffer and PBS. Purified Synj was subsequently incubated with 1 unit CaN plus 0.0125 μM calmodulin in reaction buffer (50 mM Tris (pH 7.5), 100 mM NaCl, 0.5 mM DTT, 0.025% NP-40, and 10 mM CaCl$_2$) for 1 h at 30°C. After CaN incubation, the beads were washed three times with PBS and eluted with SDS sample buffer for Western blotting. Rabbit anti p-Synj^{S1029} (1:1,000) was used to detect Synj phosphorylated at S1029 (Geng et al., 2016). Membranes were stripped (Re-Blot Plus Strong Solution; Millipore) and reprobed using rabbit HA, 1:200 (Santa Cruz Biotechnology). The extent of dephosphorylation was measured by the amount of p-Synj normalized to total Synj (anti-HA). ImageJ was used to measure the intensity of each band.

In vitro Synj phosphatidylinositol phosphatase activity assay
Synj 5′-phosphatase activity assay was previously described (Chen et al., 2014). Same protocol was used to measure Synj Sac1 phosphatase activity, except Synj was immunoprecipitated from 1 mg of protein extracts, and purified Synj was incubated with BODIPY-FL-PI(4)P (Echelon Biosciences) for 4–5 h at 30°C. Lipid products were separated by TLC and visualized under ultraviolet radiation. Phosphatase activities were determined by the ratio of lipid conversion normalized to Synj protein level. Synj levels were measured by Western blotting.

Statistics
All samples are biological repeats rather than technical repeats. For paired samples or for comparison to control groups that had been set to 1 for normalization, two-tailed Student's *t* test was used. For multiple samples, one-way ANOVA followed by Turkey post hoc test was used to determine statistical significance.

Online supplemental material
Fig. S1 shows TEM images validating the CME and CIE protocols and demonstrates that *mnb¹* enhances CIE using FM1-43 dye labeling. Fig. S2 shows that Mnb regulates SV size and suppresses ADBE. Fig. S3 demonstrates that moderate stimulation does not alter Synj phosphorylation. Fig. S4 shows the PPase activities and endophilin binding capabilities of Synj functional domain mutants. Fig. S5 shows the relative CME and Synj protein levels in *synj* function domain mutants.

References
Abeliovich, A., and A.D. Gitler. 2016. Defects in trafficking bridge Parkinson's disease pathology and genetics. *Nature*. 539:207–216. https://doi.org/10.1038/nature20414

Akbergenova, Y., and M. Bykhovskaia. 2009a. Enhancement of the endosomal endocytic pathway increases quantal size. *Mol. Cell. Neurosci.* 40:199–206. https://doi.org/10.1016/j.mcn.2008.10.005

Akbergenova, Y., and M. Bykhovskaia. 2009b. Stimulation-induced formation of the reserve pool of vesicles in Drosophila motor boutons. *J. Neurophysiol.* 101:2423–2433. https://doi.org/10.1152/jn.91122.2008

Arai, Y., T. Ijuin, T. Takenawa, L.E. Becker, and S. Takashima. 2002. Excessive expression of synaptojanin in brains with Down syndrome. *Brain Dev.* 24:67–72. https://doi.org/10.1016/S0387-7604(01)00405-3

Bonnycastle, K., E.C. Davenport, and M.A. Cousin. 2021. Presynaptic dysfunction in neurodevelopmental disorders: Insights from the synaptic vesicle life cycle. *J. Neurochem.* 157:179–207. https://doi.org/10.1111/jnc.15035

Cao, M., Y. Wu, G. Ashrafi, A.J. McCartney, H. Wheeler, E.A. Bushong, D. Boassa, M.H. Ellisman, T.A. Ryan, and P. De Camilli. 2017. Parkinson Sac

Domain Mutation in Synaptojanin 1 Impairs Clathrin Uncoating at Synapses and Triggers Dystrophic Changes in Dopaminergic Axons. *Neuron.* 93:882–896.e5. https://doi.org/10.1016/j.neuron.2017.01.019

Chanaday, N.L., M.A. Cousin, I. Milosevic, S. Watanabe, and J.R. Morgan. 2019. The Synaptic Vesicle Cycle Revisited: New Insights into the Modes and Mechanisms. *J. Neurosci.* 39:8209–8216. https://doi.org/10.1523/JNEUROSCI.1158-19.2019

Chen, C.K., C. Bregere, J. Paluch, J.F. Lu, D.K. Dickman, and K.T. Chang. 2014. Activity-dependent facilitation of Synaptojanin and synaptic vesicle recycling by the Minibrain kinase. *Nat. Commun.* 5:4246. https://doi.org/10.1038/ncomms5246

Cheung, G., and M.A. Cousin. 2013. Synaptic vesicle generation from activity-dependent bulk endosomes requires calcium and calcineurin. *J. Neurosci.* 33:3370–3379. https://doi.org/10.1523/JNEUROSCI.4697-12.2013

Cheung, G., O.J. Jupp, and M.A. Cousin. 2010. Activity-dependent bulk endocytosis and clathrin-dependent endocytosis replenish specific synaptic vesicle pools in central nerve terminals. *J. Neurosci.* 30:8151–8161. https://doi.org/10.1523/JNEUROSCI.0293-10.2010

Clayton, E.L., and M.A. Cousin. 2009a. Quantitative monitoring of activity-dependent bulk endocytosis of synaptic vesicle membrane by fluorescent dextran imaging. *J. Neurosci. Methods.* 185:76–81. https://doi.org/10.1016/j.jneumeth.2009.09.016

Clayton, E.L., and M.A. Cousin. 2009b. The molecular physiology of activity-dependent bulk endocytosis of synaptic vesicles. *J. Neurochem.* 111:901–914. https://doi.org/10.1111/j.1471-4159.2009.06384.x

Clayton, E.L., G.J. Evans, and M.A. Cousin. 2008. Bulk synaptic vesicle endocytosis is rapidly triggered during strong stimulation. *J. Neurosci.* 28:6627–6632. https://doi.org/10.1523/JNEUROSCI.1445-08.2008

Clayton, E.L., V. Anggono, K.J. Smillie, N. Chau, P.J. Robinson, and M.A. Cousin. 2009. The phospho-dependent dynamin-syndapin interaction triggers activity-dependent bulk endocytosis of synaptic vesicles. *J. Neurosci.* 29:7706–7717. https://doi.org/10.1523/JNEUROSCI.1976-09.2009

Clayton, E.L., N. Sue, K.J. Smillie, T. O'Leary, N. Bache, G. Cheung, A.R. Cole, D.J. Wyllie, C. Sutherland, P.J. Robinson, and M.A. Cousin. 2010. Dynamin I phosphorylation by GSK3 controls activity-dependent bulk endocytosis of synaptic vesicles. *Nat. Neurosci.* 13:845–851. https://doi.org/10.1038/nn.2571

Cousin, M.A., and P.J. Robinson. 2001. The dephosphins: dephosphorylation by calcineurin triggers synaptic vesicle endocytosis. *Trends Neurosci.* 24:659–665. https://doi.org/10.1016/S0166-2236(00)01930-5

Cremona, O., and P. De Camilli. 1997. Synaptic vesicle endocytosis. *Curr. Opin. Neurobiol.* 7:323–330. https://doi.org/10.1016/S0959-4388(97)80059-1

Cremona, O., G. Di Paolo, M.R. Wenk, A. Lüthi, W.T. Kim, K. Takei, L. Daniell, Y. Nemoto, S.B. Shears, R.A. Flavell, et al. 1999. Essential role of phosphoinositide metabolism in synaptic vesicle recycling. *Cell.* 99:179–188. https://doi.org/10.1016/S0092-8674(00)81649-9

Delgado, R., C. Maureira, C. Oliva, Y. Kidokoro, and P. Labarca. 2000. Size of vesicle pools, rates of mobilization, and recycling at neuromuscular synapses of a Drosophila mutant, shibire. *Neuron.* 28:941–953. https://doi.org/10.1016/S0896-6273(00)00165-3

Delvendahl, I., N.P. Vyleta, H. von Gersdorff, and S. Hallermann. 2016. Fast, Temperature-Sensitive and Clathrin-Independent Endocytosis at Central Synapses. *Neuron.* 90:492–498. https://doi.org/10.1016/j.neuron.2016.03.013

Di Paolo, G., and P. De Camilli. 2006. Phosphoinositides in cell regulation and membrane dynamics. *Nature.* 443:651–657. https://doi.org/10.1038/nature05185

Dong, Y., Y. Gou, Y. Li, Y. Liu, and J. Bai. 2015. Synaptojanin cooperates in vivo with endophilin through an unexpected mechanism. *eLife.* 4:e05660. https://doi.org/10.7554/eLife.05660

Dutta, D., C.D. Williamson, N.B. Cole, and J.G. Donaldson. 2012. Pitstop 2 is a potent inhibitor of clathrin-independent endocytosis. *PLoS One.* 7:e45799. https://doi.org/10.1371/journal.pone.0045799

Furse, S., N.J. Brooks, A.M. Seddon, R. Woscholski, R.H. Templer, E.W. Tate, P.R.J. Gaffney, and O. Ces. 2012. Lipid membrane curvature induced by distearoyl phosphatidylinositol 4-phosphate. *Soft Matter.* 8:3090–3093. https://doi.org/10.1039/c2sm07358g

Furse, S., N.J. Brooks, R. Woscholski, P.R.J. Gaffney, and R.H. Templer. 2016. Pressure-dependent inverse bicontinuous cubic phase formation in a phosphatidylinositol 4-phosphate/phosphatidylcholine system. *Chem. Data Collect.* 3-4:15–20. https://doi.org/10.1016/j.cdc.2016.08.001

Gad, H., P. Löw, E. Zotova, L. Brodin, and O. Shupliakov. 1998. Dissociation between Ca2+-triggered synaptic vesicle exocytosis and clathrin-mediated endocytosis at a central synapse. *Neuron.* 21:607–616. https://doi.org/10.1016/S0896-6273(00)80570-X

Gan, Q., and S. Watanabe. 2018. Synaptic Vesicle Endocytosis in Different Model Systems. *Front. Cell. Neurosci.* 12:171. https://doi.org/10.3389/fncel.2018.00171

Geng, J., L. Wang, J.Y. Lee, C.K. Chen, and K.T. Chang. 2016. Phosphorylation of Synaptojanin Differentially Regulates Endocytosis of Functionally Distinct Synaptic Vesicle Pools. *J. Neurosci.* 36:8882–8894. https://doi.org/10.1523/JNEUROSCI.1470-16.2016

Gormal, R.S., T.H. Nguyen, S. Martin, A. Papadopulos, and F.A. Meunier. 2015. An acto-myosin II constricting ring initiates the fission of activity-dependent bulk endosomes in neurosecretory cells. *J. Neurosci.* 35:1380–1389. https://doi.org/10.1523/JNEUROSCI.3228-14.2015

Granseth, B., B. Odermatt, S.J. Royle, and L. Lagnado. 2006. Clathrin-mediated endocytosis is the dominant mechanism of vesicle retrieval at hippocampal synapses. *Neuron.* 51:773–786. https://doi.org/10.1016/j.neuron.2006.08.029

Guimera, J., C. Casas, X. Estivill, and M. Pritchard. 1999. Human minibrain homologue (MNBH/DYRK1): characterization, alternative splicing, differential tissue expression, and overexpression in Down syndrome. *Genomics.* 57:407–418. https://doi.org/10.1006/geno.1999.5775

Guo, S., L.E. Stolz, S.M. Lemrow, and J.D. York. 1999. SAC1-like domains of yeast SAC1, INP52, and INP53 and of human synaptojanin encode polyphosphoinositide phosphatases. *J. Biol. Chem.* 274:12990–12995. https://doi.org/10.1074/jbc.274.19.12990

Guo, S., X. Zhang, M. Zheng, X. Zhang, C. Min, Z. Wang, S.H. Cheon, M.H. Oak, S.Y. Nah, and K.M. Kim. 2015. Selectivity of commonly used inhibitors of clathrin-mediated and caveolae-dependent endocytosis of G protein-coupled receptors. *Biochim. Biophys. Acta.* 1848(10, 10 Pt A):2101–2110. https://doi.org/10.1016/j.bbamem.2015.05.024

Harris, T.W., E. Hartwieg, H.R. Horvitz, and E.M. Jorgensen. 2000. Mutations in synaptojanin disrupt synaptic vesicle recycling. *J. Cell Biol.* 150:589–600. https://doi.org/10.1083/jcb.150.3.589

Haucke, V. 2005. Phosphoinositide regulation of clathrin-mediated endocytosis. *Biochem. Soc. Trans.* 33:1285–1289. https://doi.org/10.1042/BST0331285

He, K., R. Marsland III, S. Upadhyayula, E. Song, S. Dang, B.R. Capraro, W. Wang, W. Skillern, R. Gaudin, M. Ma, and T. Kirchhausen. 2017. Dynamics of phosphoinositide conversion in clathrin-mediated endocytic traffic. *Nature.* 552:410–414. https://doi.org/10.1038/nature25146

Holt, M., A. Cooke, M.M. Wu, and L. Lagnado. 2003. Bulk membrane retrieval in the synaptic terminal of retinal bipolar cells. *J. Neurosci.* 23:1329–1339. https://doi.org/10.1523/JNEUROSCI.23-04-01329.2003

Iossifov, I., M. Ronemus, D. Levy, Z. Wang, I. Hakker, J. Rosenbaum, B. Yamrom, Y.H. Lee, G. Narzisi, A. Leotta, et al. 2012. De novo gene disruptions in children on the autistic spectrum. *Neuron.* 74:285–299. https://doi.org/10.1016/j.neuron.2012.04.009

Kasprowicz, J., S. Kuenen, K. Miskiewicz, R.L. Habets, L. Smitz, and P. Verstreken. 2008. Inactivation of clathrin heavy chain inhibits synaptic recycling but allows bulk membrane uptake. *J. Cell Biol.* 182:1007–1016. https://doi.org/10.1083/jcb.200804162

Khuong, T.M., R.L. Habets, J.R. Slabbaert, and P. Verstreken. 2010. WASP is activated by phosphatidylinositol-4,5-bisphosphate to restrict synapse growth in a pathway parallel to bone morphogenetic protein signaling. *Proc. Natl. Acad. Sci. USA.* 107:17379–17384. https://doi.org/10.1073/pnas.1001794107

Klee, C.B., H. Ren, and X. Wang. 1998. Regulation of the calmodulin-stimulated protein phosphatase, calcineurin. *J. Biol. Chem.* 273:13367–13370. https://doi.org/10.1074/jbc.273.22.13367

Kononenko, N.L., and V. Haucke. 2015. Molecular mechanisms of presynaptic membrane retrieval and synaptic vesicle reformation. *Neuron.* 85:484–496. https://doi.org/10.1016/j.neuron.2014.12.016

Krebs, C.E., S. Karkheiran, J.C. Powell, M. Cao, V. Makarov, H. Darvish, G. Di Paolo, R.H. Walker, G.A. Shahidi, J.D. Buxbaum, et al. 2013. The Sac1 domain of SYNJ1 identified mutated in a family with early-onset progressive Parkinsonism with generalized seizures. *Hum. Mutat.* 34:1200–1207. https://doi.org/10.1002/humu.22372

Kuromi, H., and Y. Kidokoro. 1998. Two distinct pools of synaptic vesicles in single presynaptic boutons in a temperature-sensitive Drosophila mutant, shibire. *Neuron.* 20:917–925. https://doi.org/10.1016/S0896-6273(00)80473-0

Kuromi, H., and Y. Kidokoro. 2000. Tetanic stimulation recruits vesicles from reserve pool via a cAMP-mediated process in Drosophila synapses. *Neuron.* 27:133–143. https://doi.org/10.1016/S0896-6273(00)00015-5

Kuromi, H., and Y. Kidokoro. 2005. Exocytosis and endocytosis of synaptic vesicles and functional roles of vesicle pools: lessons from the Drosophila neuromuscular junction. *Neuroscientist.* 11:138–147. https://doi.org/10.1177/1073858404271679

Li, Y.C., and E.T. Kavalali. 2017. Synaptic Vesicle-Recycling Machinery Components as Potential Therapeutic Targets. *Pharmacol. Rev.* 69:141–160. https://doi.org/10.1124/pr.116.013342

Li, T.N., Y.J. Chen, T.Y. Lu, Y.T. Wang, H.C. Lin, and C.K. Yao. 2020. A positive feedback loop between Flower and PI(4,5)P₂ at periactive zones controls bulk endocytosis in Drosophila. *eLife.* 9:e60125. https://doi.org/10.7554/eLife.60125

Liu, S.H., M.S. Marks, and F.M. Brodsky. 1998. A dominant-negative clathrin mutant differentially affects trafficking of molecules with distinct sorting motifs in the class II major histocompatibility complex (MHC) pathway. *J. Cell Biol.* 140:1023–1037. https://doi.org/10.1083/jcb.140.5.1023

Mani, M., S.Y. Lee, L. Lucast, O. Cremona, G. Di Paolo, P. De Camilli, and T.A. Ryan. 2007. The dual phosphatase activity of synaptojanin1 is required for both efficient synaptic vesicle endocytosis and reavailability at nerve terminals. *Neuron.* 56:1004–1018. https://doi.org/10.1016/j.neuron.2007.10.032

Marks, B., and H.T. McMahon. 1998. Calcium triggers calcineurin-dependent synaptic vesicle recycling in mammalian nerve terminals. *Curr. Biol.* 8:740–749. https://doi.org/10.1016/S0960-9822(98)70297-0

McPherson, P.S., E.P. Garcia, V.I. Slepnev, C. David, X. Zhang, D. Grabs, W.S. Sossin, R. Bauerfeind, Y. Nemoto, and P. De Camilli. 1996. A presynaptic inositol-5-phosphatase. *Nature.* 379:353–357. https://doi.org/10.1038/379353a0

Mehta, S., N.N. Aye-Han, A. Ganesan, L. Oldach, K. Gorshkov, and J. Zhang. 2014. Calmodulin-controlled spatial decoding of oscillatory Ca2+ signals by calcineurin. *eLife.* 3:e03765. https://doi.org/10.7554/eLife.03765

Miller, T.M., and J.E. Heuser. 1984. Endocytosis of synaptic vesicle membrane at the frog neuromuscular junction. *J. Cell Biol.* 98:685–698. https://doi.org/10.1083/jcb.98.2.685

Nicholson-Fish, J.C., A.C. Kokotos, T.H. Gillingwater, K.J. Smillie, and M.A. Cousin. 2015. VAMP4 Is an Essential Cargo Molecule for Activity-Dependent Bulk Endocytosis. *Neuron.* 88:973–984. https://doi.org/10.1016/j.neuron.2015.10.043

O'Roak, B.J., L. Vives, W. Fu, J.D. Egertson, I.B. Stanaway, I.G. Phelps, G. Carvill, A. Kumar, C. Lee, K. Ankenman, et al. 2012. Multiplex targeted sequencing identifies recurrently mutated genes in autism spectrum disorders. *Science.* 338:1619–1622. https://doi.org/10.1126/science.1227764

Ogawa, Y., Y. Nonaka, T. Goto, E. Ohnishi, T. Hiramatsu, I. Kii, M. Yoshida, T. Ikura, H. Onogi, H. Shibuya, et al. 2010. Development of a novel selective inhibitor of the Down syndrome-related kinase Dyrk1A. *Nat. Commun.* 1:86. https://doi.org/10.1038/ncomms1090

Ori-McKenney, K.M., R.J. McKenney, H.H. Huang, T. Li, S. Meltzer, L.Y. Jan, R.D. Vale, A.P. Wiita, and Y.N. Jan. 2016. Phosphorylation of β-Tubulin by the Down Syndrome Kinase, Minibrain/DYRK1a, Regulates Microtubule Dynamics and Dendrite Morphogenesis. *Neuron.* 90:551–563. https://doi.org/10.1016/j.neuron.2016.03.027

Pauli, A., F. Althoff, R.A. Oliveira, S. Heidmann, O. Schuldiner, C.F. Lehner, B.J. Dickson, and K. Nasmyth. 2008. Cell-type-specific TEV protease cleavage reveals cohesin functions in Drosophila neurons. *Dev. Cell.* 14:239–251. https://doi.org/10.1016/j.devcel.2007.12.009

Richards, D.A., C. Guatimosim, and W.J. Betz. 2000. Two endocytic recycling routes selectively fill two vesicle pools in frog motor nerve terminals. *Neuron.* 27:551–559. https://doi.org/10.1016/S0896-6273(00)00065-9

Richards, D.A., S.O. Rizzoli, and W.J. Betz. 2004. Effects of wortmannin and latrunculin A on slow endocytosis at the frog neuromuscular junction. *J. Physiol.* 557:77–91. https://doi.org/10.1113/jphysiol.2004.062158

Rizzoli, S.O. 2014. Synaptic vesicle recycling: steps and principles. *EMBO J.* 33:788–822. https://doi.org/10.1002/embj.201386357

Rizzoli, S.O., and W.J. Betz. 2005. Synaptic vesicle pools. *Nat. Rev. Neurosci.* 6:57–69. https://doi.org/10.1038/nrn1583

Saheki, Y., and P. De Camilli. 2012. Synaptic vesicle endocytosis. *Cold Spring Harb. Perspect. Biol.* 4:a005645. https://doi.org/10.1101/cshperspect.a005645

Schuske, K.R., J.E. Richmond, D.S. Matthies, W.S. Davis, S. Runz, D.A. Rube, A.M. van der Bliek, and E.M. Jorgensen. 2003. Endophilin is required for synaptic vesicle endocytosis by localizing synaptojanin. *Neuron.* 40:749–762. https://doi.org/10.1016/S0896-6273(03)00667-6

Shaw, J.L., and K.T. Chang. 2013. Nebula/DSCR1 upregulation delays neurodegeneration and protects against APP-induced axonal transport defects by restoring calcineurin and GSK-3β signaling. *PLoS Genet.* 9:e1003792. https://doi.org/10.1371/journal.pgen.1003792

Slepnev, V.I., G.C. Ochoa, M.H. Butler, D. Grabs, and P. De Camilli. 1998. Role of phosphorylation in regulation of the assembly of endocytic coat complexes. *Science.* 281:821–824. https://doi.org/10.1126/science.281.5378.821

Soykan, T., T. Maritzen, and V. Haucke. 2016. Modes and mechanisms of synaptic vesicle recycling. *Curr. Opin. Neurobiol.* 39:17–23. https://doi.org/10.1016/j.conb.2016.03.005

Soykan, T., N. Kaempf, T. Sakaba, D. Vollweiter, F. Goerdeler, D. Puchkov, N.L. Kononenko, and V. Haucke. 2017. Synaptic Vesicle Endocytosis Occurs on Multiple Timescales and Is Mediated by Formin-Dependent Actin Assembly. *Neuron.* 93:854–866.e4. https://doi.org/10.1016/j.neuron.2017.02.011

Starkstein, S., S. Gellar, M. Parlier, L. Payne, and J. Piven. 2015. High rates of parkinsonism in adults with autism. *J. Neurodev. Disord.* 7:29. https://doi.org/10.1186/s11689-015-9125-6

Takei, K., O. Mundigl, L. Daniell, and P. De Camilli. 1996. The synaptic vesicle cycle: a single vesicle budding step involving clathrin and dynamin. *J. Cell Biol.* 133:1237–1250. https://doi.org/10.1083/jcb.133.6.1237

Tejedor, F., X.R. Zhu, E. Kaltenbach, A. Ackermann, A. Baumann, I. Canal, M. Heisenberg, K.F. Fischbach, and O. Pongs. 1995. minibrain: a new protein kinase family involved in postembryonic neurogenesis in Drosophila. *Neuron.* 14:287–301. https://doi.org/10.1016/0896-6273(95)90286-4

Uytterhoeven, V., S. Kuenen, J. Kasprowicz, K. Miskiewicz, and P. Verstreken. 2011. Loss of skywalker reveals synaptic endosomes as sorting stations for synaptic vesicle proteins. *Cell.* 145:117–132. https://doi.org/10.1016/j.cell.2011.02.039

van den Bout, I., and N. Divecha. 2009. PIP5K-driven PtdIns(4,5)P2 synthesis: regulation and cellular functions. *J. Cell Sci.* 122:3837–3850. https://doi.org/10.1242/jcs.056127

Vanhauwaert, R., S. Kuenen, R. Masius, A. Bademosi, J. Manetsberger, N. Schoovaerts, L. Bounti, S. Gontcharenko, J. Swerts, S. Vilain, et al. 2017. The SAC1 domain in synaptojanin is required for autophagosome maturation at presynaptic terminals. *EMBO J.* 36:1392–1411. https://doi.org/10.15252/embj.201695773

Verstreken, P., T.W. Koh, K.L. Schulze, R.G. Zhai, P.R. Hiesinger, Y. Zhou, S.Q. Mehta, Y. Cao, J. Roos, and H.J. Bellen. 2003. Synaptojanin is recruited by endophilin to promote synaptic vesicle uncoating. *Neuron.* 40:733–748. https://doi.org/10.1016/S0896-6273(03)00644-5

Verstreken, P., C.V. Ly, K.J. Venken, T.W. Koh, Y. Zhou, and H.J. Bellen. 2005. Synaptic mitochondria are critical for mobilization of reserve pool vesicles at Drosophila neuromuscular junctions. *Neuron.* 47:365–378. https://doi.org/10.1016/j.neuron.2005.06.018

Verstreken, P., T. Ohyama, and H.J. Bellen. 2008. FM 1-43 labeling of synaptic vesicle pools at the Drosophila neuromuscular junction. *Methods Mol. Biol.* 440:349–369. https://doi.org/10.1007/978-1-59745-178-9_26

Watanabe, S., Q. Liu, M.W. Davis, G. Hollopeter, N. Thomas, N.B. Jorgensen, and E.M. Jorgensen. 2013a. Ultrafast endocytosis at Caenorhabditis elegans neuromuscular junctions. *eLife.* 2:e00723. https://doi.org/10.7554/eLife.00723

Watanabe, S., B.R. Rost, M. Camacho-Pérez, M.W. Davis, B. Söhl-Kielczynski, C. Rosenmund, and E.M. Jorgensen. 2013b. Ultrafast endocytosis at mouse hippocampal synapses. *Nature.* 504:242–247. https://doi.org/10.1038/nature12809

Wenk, M.R., and P. De Camilli. 2004. Protein-lipid interactions and phosphoinositide metabolism in membrane traffic: insights from vesicle recycling in nerve terminals. *Proc. Natl. Acad. Sci. USA.* 101:8262–8269. https://doi.org/10.1073/pnas.0401874101

Wu, X.S., B.D. McNeil, J. Xu, J. Fan, L. Xue, E. Melicoff, R. Adachi, L. Bai, and L.G. Wu. 2009. Ca(2+) and calmodulin initiate all forms of endocytosis during depolarization at a nerve terminal. *Nat. Neurosci.* 12:1003–1010. https://doi.org/10.1038/nn.2355

Wu, X.S., Z. Zhang, W.D. Zhao, D. Wang, F. Luo, and L.G. Wu. 2014a. Calcineurin is universally involved in vesicle endocytosis at neuronal and nonneuronal secretory cells. *Cell Rep.* 7:982–988. https://doi.org/10.1016/j.celrep.2014.04.020

Wu, Y., E.T. O'Toole, M. Girard, B. Ritter, M. Messa, X. Liu, P.S. McPherson, S.M. Ferguson, and P. De Camilli. 2014b. A dynamin 1-, dynamin 3- and clathrin-independent pathway of synaptic vesicle recycling mediated by bulk endocytosis. *eLife.* 3:e01621. https://doi.org/10.7554/eLife.01621

Wu, X.S., S.H. Lee, J. Sheng, Z. Zhang, W.D. Zhao, D. Wang, Y. Jin, P. Charnay, J.M. Ervasti, and L.G. Wu. 2016. Actin Is Crucial for All Kinetically Distinguishable Forms of Endocytosis at Synapses. *Neuron.* 92:1020–1035. https://doi.org/10.1016/j.neuron.2016.10.014

Yao, C.K., Y.T. Liu, I.C. Lee, Y.T. Wang, and P.Y. Wu. 2017. A Ca2+ channel differentially regulates Clathrin-mediated and activity-dependent bulk endocytosis. *PLoS Biol.* 15:e2000931. https://doi.org/10.1371/journal.pbio.2000931

Zhang, B., Y.H. Koh, R.B. Beckstead, V. Budnik, B. Ganetzky, and H.J. Bellen. 1998. Synaptic vesicle size and number are regulated by a clathrin adaptor protein required for endocytosis. *Neuron.* 21:1465–1475. https://doi.org/10.1016/S0896-6273(00)80664-9

Zhu, Y., J. Xu, and S.F. Heinemann. 2009. Two pathways of synaptic vesicle retrieval revealed by single-vesicle imaging. *Neuron.* 61:397–411. https://doi.org/10.1016/j.neuron.2008.12.024
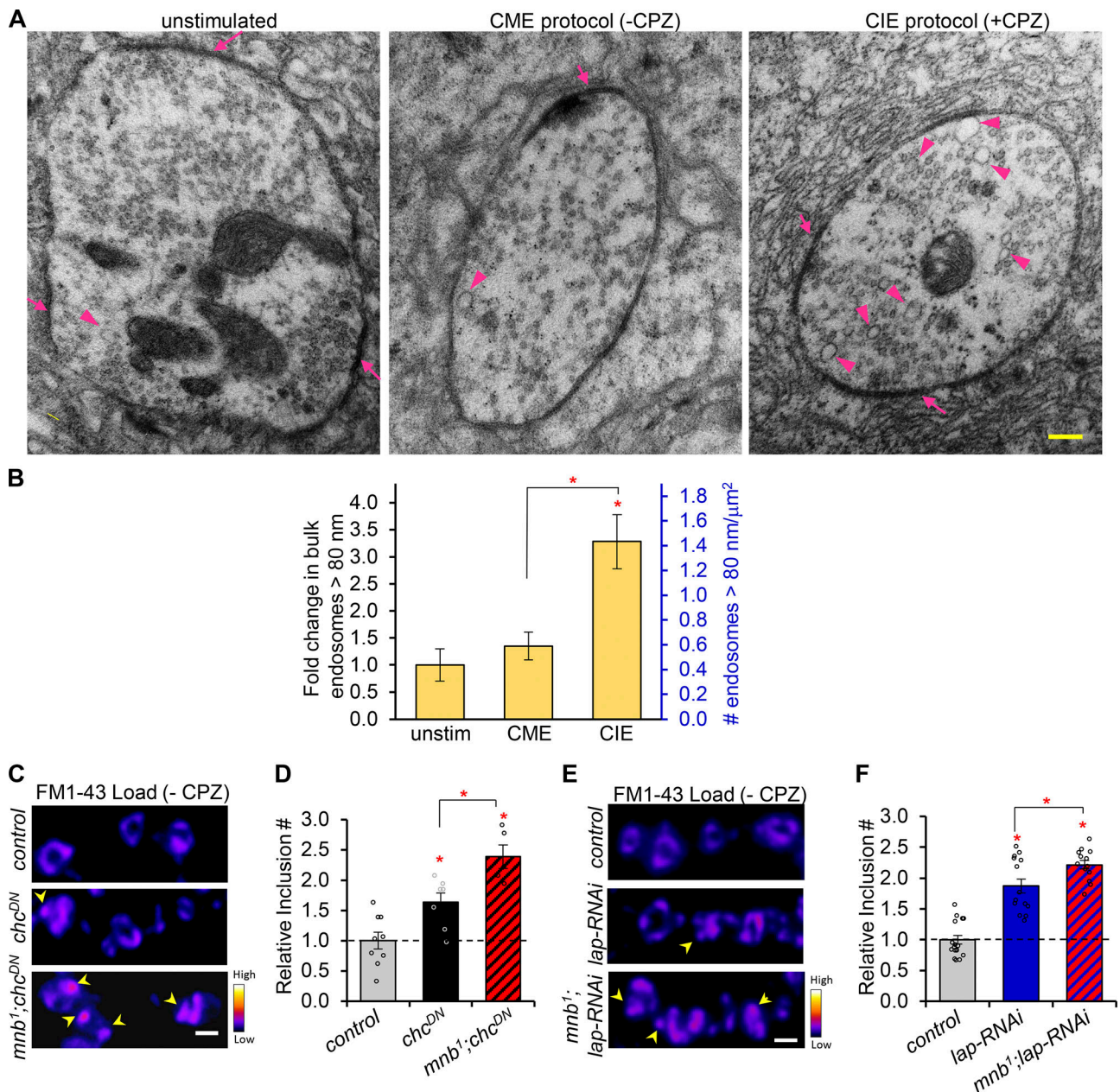
Supplemental material

Figure S1. **CIE protocol activates bulk endocytosis; *mnb[1]* enhances CIE. (A)** TEM images of synaptic boutons from wild-type NMJs stimulated by the indicated conditions. Arrowheads indicate bulk-like cisternae >80 nm in diameter. Arrows point to synaptic thickenings in the active zone area. Scale bar = 200 nm. **(B)** Quantification of bulk-like cisternae. Left y axis shows fold-change, and right y axis shows the number of bulk endosomes >80 nm normalized to bouton area. *n* = 18, 16, and 19 for unstimulated, CME, and CIE protocols, respectively. **(C and E)** FM1-43 load following KCl stimulation (pseudo-colored). Arrowheads point to membrane inclusions indicative of bulk endocytosis. **(D and F)** Relative number of boutons with FM1-43 inclusions normalized to total bouton number. For B, *n* = 9 NMJs for control, 7 for *chc^DN*, and 5 for *mnb[1]; chc^DN*. For D, *n* = 18 NMJs for control, 14 for *lap-RNAi*, and 13 for *mnb[1];lap-RNAi*. *, P < 0.05 compared with control or as indicated. Scale bar = 2 µm. All values are mean ± SEM.
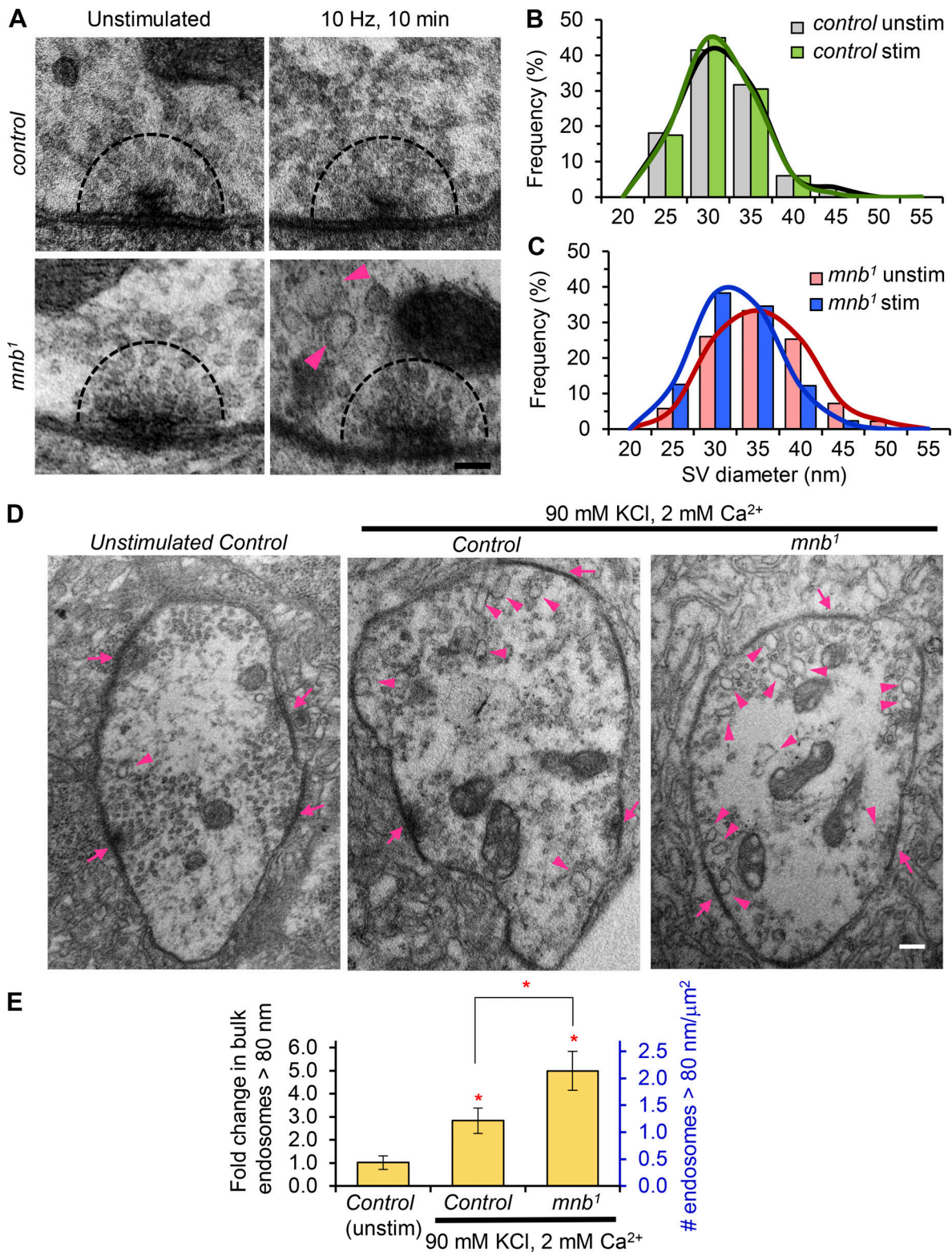
Figure S2. **Mnb regulates SV size and suppresses ADBE. (A)** TEM images of the active zone area. SV within 200-nm radius (dashed semicircle) of the T-bar were examined to determine SV size. Arrowhead highlights the bulk cisternae observed following stimulation. Scale bar = 100 nm. **(B and C)** SV diameter distribution for *control* in B and *mnb1* in C, with and without 10-Hz, 10-min stimulation (stim). For control unstimulated (unstim), $n = 24$; stimulated, $n = 18$ active zones. For *mnb1*, unstimulated, $n = 11$; stimulated, $n = 14$ active zones. **(D)** Representative TEM images of synaptic boutons. 90 mM KCl/2 mM Ca^{2+} stimulation for 10 min was used to trigger ADBE. Arrowheads indicate bulk-like cisternae >80 nm in diameter. Arrows point to synaptic thickenings in the active zone area. Scale bar = 200 nm. **(E)** Quantification of bulk-like cisternae. Left y axis shows fold-change, and right y axis shows the number of bulk endosomes >80 nm normalized to bouton area. *, P < 0.05 compared with unstimulated control or as indicated. For unstimulated control, $n = 18$; for stimulated control, $n = 18$; for stimulated *mnb1*, $n = 14$. All values are mean ± SEM.

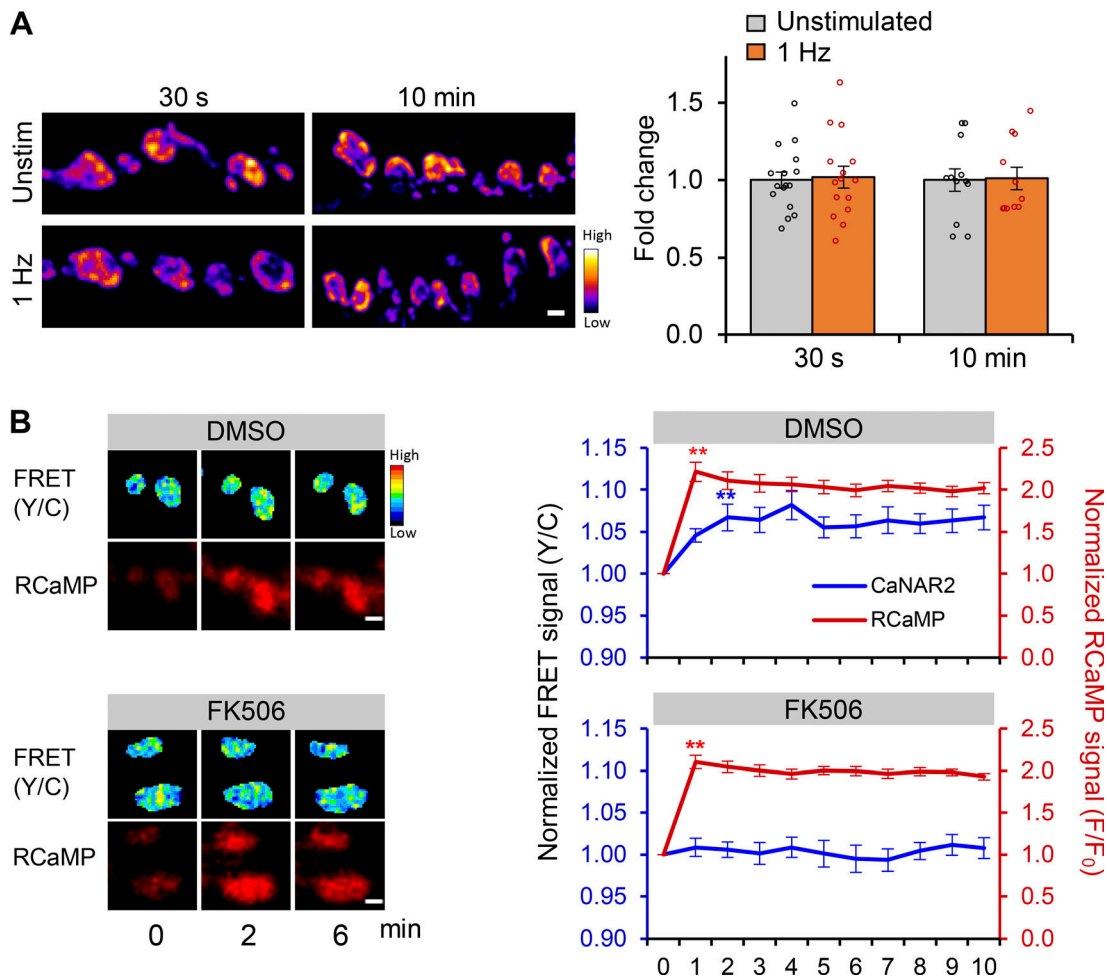Figure S3. **1-Hz stimulation does not affect the level of pSynj. (A)** Pseudo-colored images of pSynj staining intensity in unstimulated and 1-Hz stimulated NMJs for the indicated time frame. Graph shows quantification of fold-change in pSynj intensity by comparing to unstimulated NMJ (for 30 s, n = 16 NMJ for unstimulated; n = 15 NMJ for 1 Hz; for 10 min, n = 12 NMJ for unstimulated; n = 11 NMJ for 1 Hz). **(B)** Time-course images of NMJs expressing FRET-based CaN activity reporter, cyto-CaNAR2 (pseudo-colored), and Ca^{2+} indicator RCaMP during indicated stimulations. NMJs were treated with either DMSO as vehicle control or 10 μM FK506 before 10-Hz stimulation for 10 min. FK506, a selective CaN inhibitor, effectively blocked the increase in CaNAR2 FRET signal but did not alter Ca^{2+} influx, suggesting that the CaNAR2 sensor is reliably reporting CaN activity. n = 13 NMJs for DMSO and 16 for FK506. **, $P < 0.05$ compared with t = 0 from that time point on. Scale bar, 2 μm. All values are mean ± SEM.
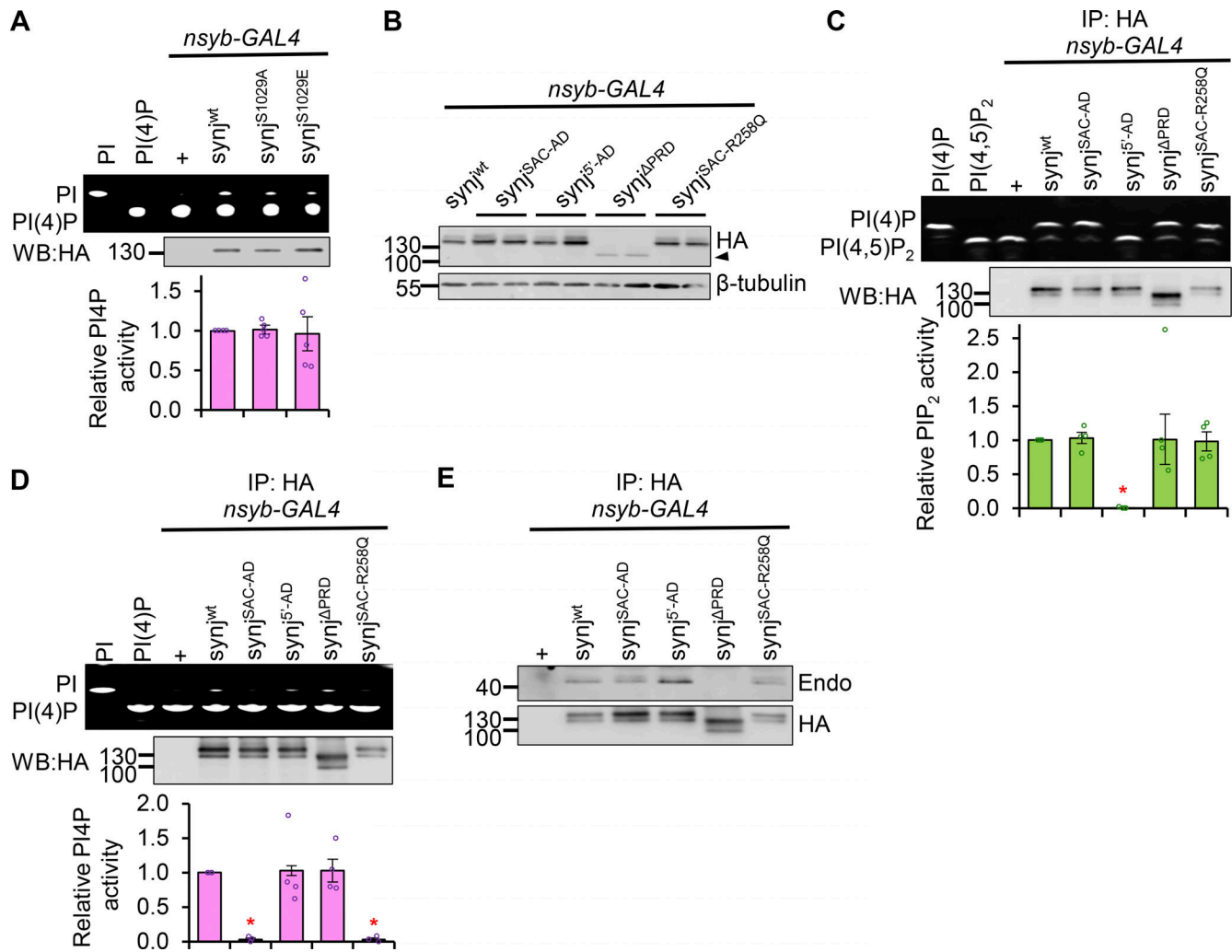
Figure S4. **Synj functional domain mutants and their PPase activities and endophilin-binding capabilities. (A)** SAC1 activity remains unchanged in phosphomimetic and phospho-null Synj mutants. SAC1 activity is determined by measuring the amount of PI generated from PI(4)P and normalizing to the amount of immunoprecipitated Synj. Values are shown as fold-change normalized to control. $n = 5$ independent experiments. **(B)** Western blot demonstrating levels of HA-tagged Synj mutant protein. synj$^{\Delta PRD}$ shows reduced level of truncated Synj (arrowhead). β-Tubulin is used as loading control. **(C)** synj$^{5'-AD}$ does not have a functional 5'-PPase domain to convert PI(4,5)P$_2$ to PI(4)P. PIP$_2$ activity is determined by measuring the amount of PI(4)P generated from PI(4,5)P$_2$, followed by normalization to the amount of immunoprecipitated (IP) Synj detected by Western blot (WB). $n = 4$ independent experiments. **(D)** SAC1 activity is abolished in synj^{SAC-AD} and synj$^{SAC-R258Q}$. Values are shown as fold-change normalized to control. $n = 4$ independent experiments. In C and D, *, P < 0.05 compared with control. **(E)** Representative Western blot showing interaction between Synj and endophilin is blocked in synj$^{\Delta PRD}$. HA antibody detects the amount of Synj protein in the IP.
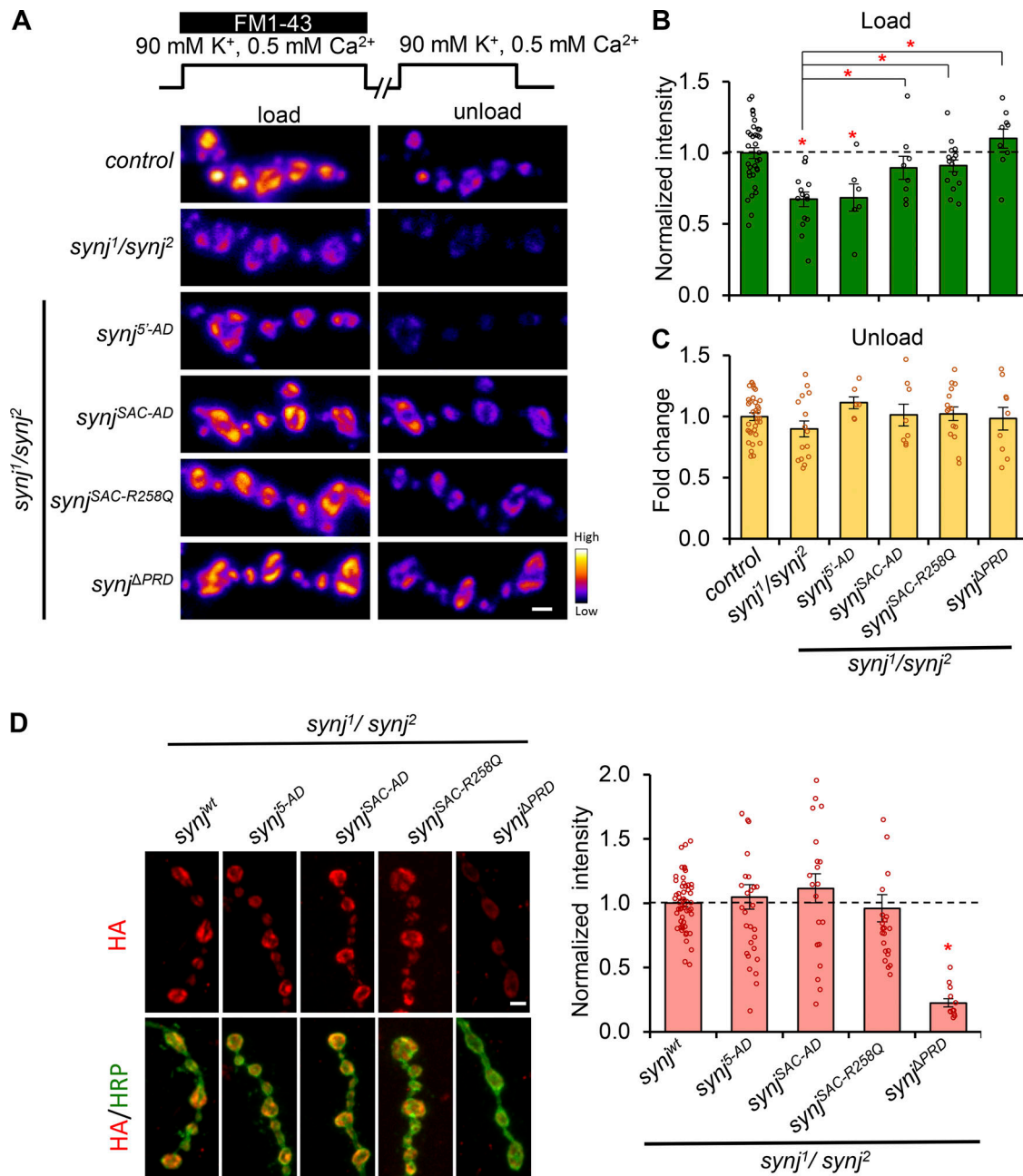
Figure S5. **CME and synaptic Synj protein levels in *synj* function domain mutants. (A)** Images of NMJ loaded and unloaded with FM1-43 for the indicated genotypes in *synj[1]/synj[2]* background. 1 min of high K^{+} stimulation in 0.5 mM Ca^{2+} was used to load vesicles taken up by CME, and 30-s stimulation was used to unload FM1-43. **(B)** Relative FM1-43 loading intensities were normalized to control NMJ. **(C)** Fold-change in FM1-43 dye unload was determined by $\Delta F/F_{load}$ and then normalized to control NMJ. For B and C, control = 34; *synj* mutant = 15. In *synj* mutant background: *synj[5'-AD]*, $n = 6$; *synj[SAC-AD]*, $n = 8$; *synj[SAC-R258Q]*, $n = 15$; *synj[ΔPRD]*, $n = 9$. **(D)** Representative images of NMJs stained with HA (red) to demonstrate the presynaptic localization of HA-tagged Synj functional domain mutant proteins. HRP (green) was stained to outline presynaptic bouton membranes (*synj[wt]*, $n = 54$; *synj[5'-AD]*, $n = 30$; *synj[SAC-AD]*, $n = 22$; *synj[SAC-R258Q]*, $n = 23$; *synj[ΔPRD]*, $n = 13$). Scale bar = 2 μm in A and D. *n* value indicates the number of NMJs examined. All values are mean ± SEM. *, P < 0.05 compared with control NMJ or as indicated.

Peng et al.
Molecular mechanism coordinating endocytosis modes

Journal of Cell Biology   S5
https://doi.org/10.1083/jcb.202011028